The Pennsylvania State University

The Graduate School

INVESTIGATION OF THE OPTOELECTRONIC PROPERTIES OF FORMAMIDINIUM LEAD BROMIDE PEROVSKITES USING TIME-RESOLVED INFRARED SPECTROSCOPY

A Thesis in

Chemistry

by

John R. Swartzfager

Submitted in Partial Fulfillment
of the Requirements
for the Degree of

Master of Science

December 2019

The thesis of John R. Swartzfager was reviewed and approved* by the following:

John Asbury
Professor of Chemistry
Thesis Advisor

Mark Maroncelli
Distinguished Professor of Chemistry

Ben Lear
Associate Professor of Chemistry

Chris Giebink
Associate Professor of Electrical Engineering

Philip C. Bevilacqua
Distinguished Professor of Chemistry and Biochemistry and Molecular Biology
Head of the Chemistry Department

*Signatures are on file in the Graduate School

ABSTRACT

Halide perovskite photovoltaics have garnered a significant amount of interest over the last ten years. With favorable optoelectronic properties including high open circuit voltages, efficient PL quantum yields, and low non-radiative recombination rates, combined with solution processability and recent efficiencies of 24.2%, perovskites are serious contenders to compete with silicon photovoltaics. However, an in-depth understanding of the materials excited state properties and why they can achieve such high efficiencies is missing. Which is why previous work by our lab sought to better understand the excited state dynamics of methylammonium lead iodide ($MAPbI_3$), using time-resolved infrared spectroscopy. On the basis of that work it was discovered that charge carriers present in $MAPbI_3$ interact with the phonon modes of the material, which leads to the formation of large polarons. These large polarons are responsible for the long lived excited state lifetimes and modest charge carrier mobility's of the material.

Upon completion of the $MAPbI_3$ study we decided to study a different halide perovskite, with the hopes of determining our labs previous observations were unique to $MAPbI_3$, or if they were a universal property of all halide perovskites. The material decided upon was formamidinium lead bromide ($FAPbBr_3$). This choice was influenced by recent interest in formamidinium perovskites, as it had been discovered they possessed a superior thermal stability to that of methylammonium perovskites. The focus of this thesis is on the study of the optoelectronic properties of $FAPbBr_3$, utilizing time-resolved infrared spectroscopy. From our investigation it was discovered that the charge carriers of $FAPbBr_3$ form large polarons, which have a similar binding energy to those of $MAPbI_3$. Also, while probing the structural dynamics of $FAPbBr_3$, a unique form of coupling was revealed. It was discovered that the transient C-N stretch of the organic cation, and the higher energy Drude-like absorption tail of the polaron formed a Fano resonance. This unique resonance occurs due to coupling between a discrete and continuum state, which to our knowledge is the first time such a phenomenon has been observed

for $FAPbBr_3$. Fitting the Fano resonance allowed for the extraction of the transient line shape of the C-N stretch, the breadth of which was discovered to increase at higher temperature. This phenomenon was previously observed for the transient N-H bend of $MAPbI_3$, implying that there is an increased dynamic disorder at higher temperature, leading to an increased population of large polarons. However, the center frequency of the transient C-N stretch did not change with temperature, a characteristic not observed for the transient N-H bend of $MAPbI_3$. Implying that the dynamics of the two different cations may respond differently to temperature, which we hope to address in future studies using polarization selective infrared pump-probe spectroscopy.

TABLE OF CONTENTS

LIST OF FIGURES

LIST OF ABBREVIATIONS

Al_2O_3	Aluminium oxide
Br^-	Bromide
CaF_2	Calcium fluoride
$CaTiO_3$	Calcium titanate
Cs^+	Cesium cation
CVD	Chemical vapor deposition
Cl^-	Chloride
DMSO	Dimethyl sulfoxide
ESA	Excited State Absorption
FA^+	Formamidinium cation
$FAPbI_3$	Formamidinium lead iodide
$FAPbBr_3$	Formamidinium lead bromide
FWHM	Full width half max
FABr	Formamidinium bromide
FTIR	Fourier transform infrared
GSB	Ground state bleach
IR	Infrared
I^-	Iodide
IPA	Isopropyl alcohol
$PbBr_2$	Lead(II) bromide
Pb^{2+}	Lead cation
LO	Longitudinal optical
MCT	Mercury cadmium telluride

MA^+	Methylammonium cation
$MAPbBr_3$	Methylammonium lead bromide
$MAPbI_3$	Methylammonium lead iodide
Mid-IR	Mid-infrared
MD	Molecular dynamics
Nd:YAG	Neodymium-doped yttrium aluminum garnet
PL	Photoluminescence
TRIR	Time-resolved Infrared
TRVis	Time-resolved visible
Sn^{2+}	Tin Cation
TPPO	Triphenylphosphine oxide
UV-Vis	Ultraviolet-Visible

ACKNOWLEDGEMENTS

To begin with I would like to thank my advisor, Dr. John Asbury. Who has allowed me the freedom to pursue research which I genuinely enjoy and find interesting. I would also like to thank him for the opportunities he has afforded me, and for the insightful discussions we have had during our meetings.

Next I would like to thank the members of the Asbury lab, Kyle, Grayson, Eric, and Kelsey. Who I have had the pleasure of working with for the last few years. I have learned so much about science and research through our interactions, and for that I am truly grateful. But it is the friendship that we all share which I truly appreciate the most. It is this friendship which makes me look forward to coming to work, and makes this lab truly feel like a family.

I would also like to thank the members of my committee, Dr. Ben Lear, Dr. Mark Maroncelli, and Dr. Chris Giebink, for the advice and help they have provided me with while at Penn State.

I would also like to thank my undergraduate advisor, Dr. Kelley Donaghy. Who helped guide me as I worked through undergrad, and for suggesting I should go to graduate school.

I would also like to thank my high school chemistry teacher, Mrs. Heather Pero. It was her enthusiasm for the subject and her teaching which made me fall in love with and pursue a career in chemistry.

Finally I would like to thank my Mom, Dad, and sister. I appreciate everything you have done for me, more than you could imagine. Thank you for your support and believing in me, even during the times I didn't believe in myself. I don't know how I would have gotten through college and graduate school without your love, support, and understanding. Thank you for everything.

Chapter 1: Introduction

Approximately 85% of the worlds power needs are met by fossil fuels.[1] With these resources becoming ever scarcer, and the prediction that our power needs will double by the year 2050, the need to find renewable sources of energy is becoming more important each passing year.[1] The average amount of solar flux reaching the earth's surface is ~170 W/m^2.[2] Even if only 10% of this flux could be converted to useable electricity, a location with an area only 0.1% that of the earth, could supply all of the worlds energy needs.[3] In order to harvest this sunlight we can use solar thermal systems, which use the sun to drive heat engines.[2] Or through the use of solar cells, which absorb the sunlight and convert it to electricity.[2]

The most common type of solar cells are produced using silicon, which have a theoretical efficiency of ~31% based off the Shockley-Queisser limit for a single junction device.[4-7] There are three main forms of silicon used to produce solar cells, which include monocrystalline, polycrystalline, and amorphous.[4, 7-10] Monocrystalline silicon creates the most efficient single junction devices, with a record efficiency of 26.7% and commercial cells in the 15-22% range.[8, 10-11] Monocrystalline silicon is commonly made using the Czochralski process, which involves slowly pulling a seed crystal from a vat of molten silicon.[12] This slow pulling allows for a large single crystal ingot to be produced.[12] However, because of this slow pulling process, monocrystalline silicon is the most expensive and time consuming form to produce.[12] Polycrystalline silicon has a single junction record efficiency of 22.3% and commercial cells are typically in the 12-15% range.[8, 10-11] Polycrystalline silicon is formed mainly using directional solidification, in which silicon is melted and allowed to solidify in one direction.[12] Directional solidification is cheaper than the Czochralski process, but produces lower purity ingots.[12] Finally, amorphous silicon creates the least efficient devices, with a record efficiency of 10.2% and

commercial cells in the 6-7% range.[8, 10-11] Amorphous silicon is commonly produced by chemical vapor deposition (CVD) of silanes, and doesn't require the high temperatures used in the production of ingots, allowing for deposition to run from room temperature up to 400 °C.[12-13] The use of CVD allows for amorphous silicon films to be grown on a variety of substrates including glass, metal, and plastic.[11] However, this process also produces samples with the highest number of impurities and the lowest efficiencies.[7]

The processing of silicon into ingots or films makes up a significant portion of the cost to manufacture silicon solar cells.[14] While we now have the infrastructure to produce silicon on an industrial scale, expanding these operations to supply a significant portion of our energy needs would be too complex and costly, as it would require orders of magnitude more scale-up.[9, 15-16] Due to the complexity and cost of such a scale-up alternatives to silicon have been investigated. These alternatives should ideally have similar efficiencies and be solution processable. The solution processability would allow for easy scalability and continued growth once established, using techniques such as roll-to-roll printing, screen printing, or ink jet printing.[16] Both solution processability and high efficiencies are characteristics held by the rapidly growing field of perovskite photovoltaics.[16-17]

Perovskite Photovoltaics

The reason for the interest in perovskites as photovoltaic materials is due in part to their optoelectronic properties, including long lived excited states, high open circuit voltages, low non-radiative recombination rates, and efficient PL quantum yields.[16, 18-20] These properties, along with solution processability and bandgap tunability have made halide perovskites an attractive candidate for non-silicon based photovoltaics.[16, 20] The interest in halide perovskites was what lead to the rapid growth in efficiency, from a modest 3.8% in 2009 up to an impressive 24.2% as of

2019, making it one of the fastest growing photovoltaic materials and a serious contender to compete with silicon.[8, 16, 20-21]

Perovskite photovoltaics borrow their name from a group of minerals discovered by Gustav Rose and named after the Russian mineralogist, L.A. Perovski.[22-23] The first compound placed into this class was calcium titanate ($CaTiO_3$), after its discovery in 1839.[22-23] A material is defined as a perovskite if it shares the same crystal structure as $CaTiO_3$, which is often presented as the simple chemical formula of ABX_3.[17-18, 23] In the case of perovskite photovoltaics the monovalent A site cation is often an organic molecule, such as methylammonium (MA^+) or formamidinium (FA^+) (although cesium (Cs^+) is sometimes used to produce fully inorganic perovskites). The divalent B site cation is typically lead (Pb^{2+}), however tin (Sn^{2+}) has been used with varying degrees of success (the problem being that tin is more easily oxidized than lead). Finally, the monovalent X anion is typically a halide, such as iodide (I^-), bromide (Br^-), or chloride (Cl^-).[17-18, 22-23] The structure of a perovskite as shown in **Figure 1-1** is best depicted as a 3D network of B cations octahedrally coordinated to X anions (BX_6), with an A cation at the center of the cuboctahedral space created by the BX_6 network.[17-18, 23]

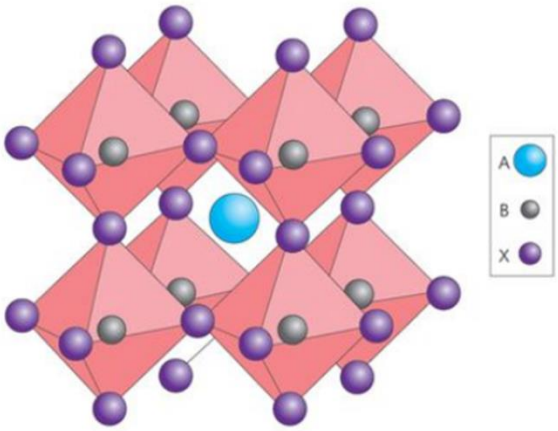

Figure 1-1: Cubic perovskite structure. Adapted from reference 17.

In order for a stable perovskite to be formed the A site cation must be the right size to fill the cuboctahedral space created by the BX_6 octahedra. If the A site cation is too large or small then the sample will not form the perovskite structure, instead a material with different optoelectronic properties is produced.[17-18, 24] In order to predict the stability of perovskites a relation between the

ionic radii of the A, B, and X ions referred to as the Goldschmidt tolerance factor, shown as equation 1-1, can be used.[18, 24]

$$t = \frac{r_A + r_X}{\sqrt{2}(r_B + r_X)} \qquad (1\text{-}1)$$

Where r_A, r_B, and r_X are the ionic radii of the A, B, and X site ions respectively. Based upon experimentation it has been found that stable perovskites are typically produced when the value of t is between 0.75 and 1. This tolerance range means the A site cation can be on the smaller side and still form the perovskite structure, but will not form if on the larger side.[18, 24] The A site cations which have been found to work are MA^+, FA^+, and Cs^+, with the most commonly used cation being MA^+.[16, 25]

The electronic structure of perovskites arises primarily from the atoms which comprise their inorganic framework.[26-27] In the case of $MAPbI_3$, it has been shown via DFT calculations that the valence band is formed predominantly from the 5P orbitals of I^- and 6s orbitals of Pb^{2+}, while the conduction band is formed from the 6P orbitals of Pb^{2+}.[26] When a photon with the appropriate wavelength is absorbed by a perovskite, an electron is excited to the conduction band and a hole is left in the valence band. Initially the electron and hole are coulombically bound and form a quasiparticle known as an exciton.[28-30] However, due to the low exciton binding energy of halide perovskites at room temperature (~10meV), the exciton will rapidly dissociate into electrons and holes.[30-31] It is believed that these charge carriers interact with the phonon modes of the polarizable perovskite lattice, causing the surrounding lattice to distort around a charge carrier, as depicted in **Figure 1-2**.[29, 32-34] This distortion causes the charge

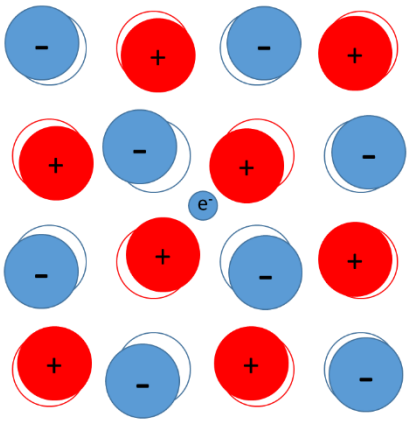

Figure 1-2: Large polaron formed by presence of conduction band electron. Outlines represent positions of ions before introduction of electron, while Filled circles represent positions of ions in presence of electron.

carrier to become self-trapped, producing a quasi-particle known as polaron.[35-36] Depending on whether the distortions are long range and spread out over many lattice sites, or short range and restricted to one lattice site determines whether large or small polarons form respectively.[35] On the basis of first principles calculations it has been theorized that long range interactions dominate, which should lead to the formation of large polarons on the sub-picosecond timescale following photoexcitation.[33] However, while the presence of large polarons in halide perovskites has been inferred from the first principle calculations mentioned above, direct observation of these states have remained elusive.

This lack of experimental evidence for large polaron formation in halide perovskites led to previous work in our lab, which focused on studying $MAPbI_3$ perovskites using time-resolved infrared (TRIR) spectroscopy, as large polarons have a unique spectroscopic signature in the mid-infrared (mid-IR).[37-38] Through the use of TRIR spectroscopy it was discovered that $MAPbI_3$ has a broad absorption feature present between 1100 to 4000 cm^{-1}, with an absorption maximum at 1200 cm^{-1}.[37-38] A large polaron absorption model developed by Emin was used to fit the data, which uses a hydrogenic model to describe the interaction of a charge carrier with the polarization cloud caused by lattice distortions (**Figure 1-3**).[35, 37-38] Based on Emin's model, the self-trapping energy of a large polaron is predicted to equal $-E_p$ and is the result of three contributions.[35, 37-38] The first contribution is the increase in kinetic energy of the charge carrier upon localization, which provides an energy of E_p. A second contribution of $-4E_p$ is provided by the lowering in energy of the charge carrier, and a final

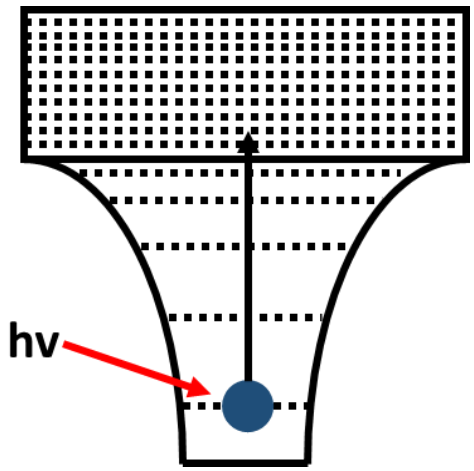

Figure 1-3: Photoionization of polaron into continuum of unbound states.

contribution of $2E_P$ is provided by the energy required to distort the nuclei from their equilibrium positions.[35, 37-38] However, the peak maximum obtained from a large polaron spectrum actually corresponds to three times the polaron binding energy, this is because in order to photoexcite into a continuum of unbound states both, the self-trapping energy (E_P), and the nuclear distortion energy ($2E_P$) must be overcome.[35, 37-38] The absorption maximum produced by $MAPbI_3$ at 1200 cm^{-1} corresponds to a polaron binding energy of 0.05eV.[37-38] In order to use the large polaron model to fit the data the wave vector, k, for the charge carrier in an unbound continuum state must be calculated, the equation to do so can be seen below as equation 1-2.[35, 37-38]

$$k = \sqrt{\frac{2m(\hbar\omega - 3E_p)}{\hbar}} \qquad (1\text{-}2)$$

Where m is the mass of the charge carrier in the continuum state, ω is the frequency of light used to photoionize the charge carrier, and ħ represents the reduced Planck's constant. Treating the absorption event akin to that of the photoelectric effect, by treating the final-state wave function as a free carrier, and implementing Fermi's Golden Rule leads to equation 1-3.[35, 37-38]

$$\frac{a}{n_p} = \frac{128\pi e^2}{3m\omega c}\frac{kR^3}{[1+(kR)^2]^4} \qquad (1\text{-}3)$$

Where a/n_p represents the absorption coefficient per density of polarons, e is the elementary charge, c is the speed of light and R is the effective delocalization length of the polaron. Through the use of temperature dependent TRIR measurements, it was discovered that as the temperature of the system was lowered, the effective delocalization length of the polaron was increased (**Figure 1-4A)**.[37-38] Because the distortions of the nuclear framework are what lead to the formation of polarons, analysis of the vibrational dynamics of MA^+ in the presence of charge carriers was carried out.

Since the orbitals of MA^+ do not contribute to the band-gap of the perovskite, any change in vibrational dynamics would be due to variations in its local environment.[26, 37-38] The transient vibrational spectra of the N-H bend, at various temperatures, was used to observe the effect a charge carrier had on the inorganic lattice.[37-38] As the temperature decreased, the center frequency of the N-H bend blue shifted relative to its vibration in the absence of a charge carrier (**Figure 1-4B)**.[37-38] Previous work had shown that a blue shift in the N-H bend was due to weakening of the hydrogen bonding interactions between the N-H moiety, and the lattice.[39-40] There was also a change in the full width half max (FWHM) of the transient vibrational feature, it was observed that as the temperature was lowered the FWHM decreased.[37-38] This decrease in FWHM was discovered to occur due to larger amplitude and higher frequency fluctuations of the inorganic lattice, which would lead to an increased vibrational dephasing time.[37-38] The dephasing time of a molecular vibration indicates how long a collection of vibrational modes in a sample will keep their initial phase with respect to each other. Larger amplitude fluctuations of the perovskite lattice could lead to increased chances of the organic cation undergoing elastic collision, which can cause a vibration to lose its initial phase. This information lead to the conclusion that the changes in the transient

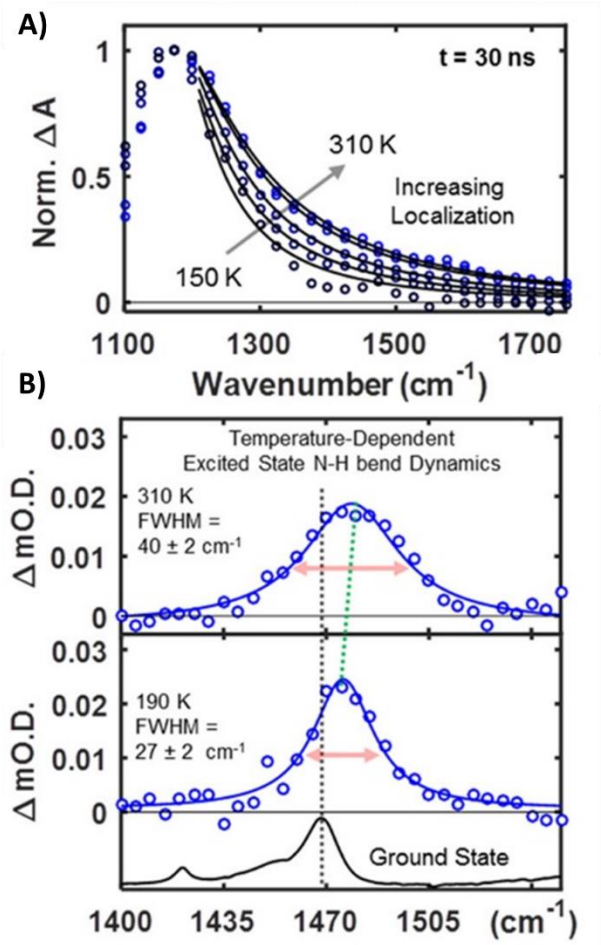

Figure 1-4: A) Polaron TRIR spectrum of $MAPbI_3$ with large polaron model overlaid at various temperatures. **B)** TRIR spectra of $MAPbI_3$ bend at 310 K and 190 K after polaron subtraction. Adapted from reference 36.

vibrational mode, as temperature increased, were due to the increased fluctuations of the inorganic lattice, a more in-depth discussion of which will be covered in chapter 4.[37-38]

Upon completion of the $MAPbI_3$ study we sought to use TRIR spectroscopy to study a different halide perovskite. We decided on $FAPbBr_3$ for a number of reasons, the first being that there was recent interest in FA^+ perovskite variants, as it had been discovered that they possess better thermal stability than MA^+, making them more ideal candidates for solar cells.[41] The second reason was the interest in creating tandem cells using halide perovskite, which can be accomplished by creating perovskite cells with different X site anions.[17, 20] Thus investigating the charge carrier dynamics of a material, which could absorb the high energy photons of the solar spectrum, would be of interest to the photovoltaic field.[17, 20] Also, investigating $FAPbBr_3$ would allow us to compare and contrast its charge carrier properties to that of $MAPbI_3$, allowing us to see if our lab's previous observations were unique to $MAPbI_3$, or more universal to lead halide perovskites as a whole.

The focus of this thesis is the investigation of the charge carrier properties of $FAPbBr_3$ thin films using TRIR spectroscopy. By comparing these results to those of $MAPbI_3$, we hope to gain an understanding of the role that polarons play in new types of perovskite materials, which have improved thermal stabilities and complementary optical properties to that of $MAPbI_3$. This thesis is broken up into the following chapters. Chapter 2 goes over the experimental techniques used, including sample preparation, as well as the basics of TRIR spectroscopy. Chapter 3 goes over spectroscopic line shapes, the comprehension of which is required to understand the analysis of the data presented in this thesis. Chapter 4 presents the data and conclusions obtained from this project. Finally, Chapter 5 presents the future directions for this project, including a number of experiments which would assist in further verifying our interpretations of the data.

Chapter 2: Experimental Methods

This chapter will focus on the methods used to produce the samples studied, including substrate preparation and thin film deposition. Along with this the spectroscopic methods used to characterize the samples will be described.

Sample Preparation

Substrate Preparation

The type of substrate used differed based on the analysis being performed. For measurements in the ultraviolet and visible region glass slides were used, while for the mid-IR calcium fluoride (CaF_2) was used. Substrates were cleaned by sonication for 10 minutes each in the following solvents, distilled water, methanol, acetone, and isopropyl alcohol (IPA). After sonication in IPA, the substrates were blown dry with a stream of nitrogen and then placed into a UV ozone cleaner for 10 minutes. Following ozone treatment, approximately 1 mL of a 5 weight percent aluminum oxide (Al_2O_3) in IPA solution was spun onto the substrate at 6000 rpm for 20 seconds. Once the substrates were coated they were placed into a kiln and heated to 450 °C for 1 hour.

$FAPbBr_3$ Thin Film Preparation

Approximately 100 mg of formamidinium bromide (FABr) and 34 mg of lead (II) bromide ($PbBr_2$) were dissolved in 500 µL of dimethyl sulfoxide (DMSO) to produce a 0.55 M solution. This solution was allowed to stir at 30°C for 15 minutes, until all solids had fully dissolved. Once dissolved, 150 µL of the solution was spread onto an Al_2O_3 coated substrate, directly after which the sample was spun using a three step spinning process, in which the sample was spun at 500, 1000, and 3000 rpm for 10, 40, and 40 seconds respectively. Within the first 5 seconds of the 3000 rpm spin coating process a solution consisting of 34 mg of triphenylphosphine oxide (TPPO)

in 35 mL of toluene was dripped, at a constant rate, onto the sample for approximately 2 seconds. The toluene acted as an anti-solvent, allowing for the creation of films with a uniform morphology.[42] While the TPPO allowed for passivation of the perovskite surface, reducing the number of defects and dangling bonds.[43-45] This passivation is believed to occur by donation of electrons from the oxygen, in TPPO, to uncoordinated Pb^{2+} in the lattice.[46] It is important when carrying out the TPPO drip to keep the syringe tip as close to the substrate as possible without letting it touch. An effort should also be made to make sure air bubbles are not expelled during the TPPO drip. Either of these can lead to the streaks or swirls, which can ruin the surface quality of the film. Following spin coating, the film was annealed at 120°C for 10 minutes and then allowed to cool to room temperature.

Characterization Techniques

Ultraviolet-Visible (UV-Vis) Spectroscopy

A Beckman DU 520 spectrometer was used to make steady state UV-Vis measurements. The spectrometer was setup to measure between 400 and 850 nm with 1 nm steps. Before measurements were made the instrument was blanked with the appropriate substrate, for example if measuring $FAPbBr_3$ on Al_2O_3 coated glass, a piece of Al_2O_3 coated glass was used as a blank. After the blank was taken the sample was placed into the sample holder and the spectrum was collected.

Time-Resolved Infrared Spectroscopy

Time-resolved infrared (TRIR) spectroscopy is a pump-probe technique, which involves monitoring the change in absorption (ΔA) of an infrared probe, in time, following photoexcitation of the sample using a short laser pulse. Since the probe lies in the mid-IR region of the electromagnetic spectrum, the transitions observed are typically due to changes in the vibrational

dynamics of the materials. However, certain electronic transitions, such as intraband transitions of quantum dots or excitation of trapped charge carriers, can be observed.[47-49] Probing molecular vibrations can allow for easier interpretation of data when compared to other pump-probe techniques, such as time-resolved visible (TRVis) spectroscopy, which uses a visible pump and visible probe.[47] Analysis of TRVis spectra can be challenging, as electronic transitions typically have broad line widths, making interpretation of multiple peaks difficult.[47] This is in contrast to TRIR spectroscopy, which has the potential to probe vibrations.[47] Vibrations typically have narrow line shapes and are dependent on molecular functionalities, which can be tailored to distinguish multiple species in a single sample.[47]

Since TRIR is a difference technique, the sign of ΔA can be positive or negative, depending on the type of transition being probed.[47, 50] For example, photoexcitation of a sample reduces the ground state population of species, if this photoexcitation results in a change of the vibrational frequency, then a signal with a negative amplitude will be observed at the location of the ground state vibration. This type of signal is termed a ground state bleach (GSB).[47, 50] Conversely, since a

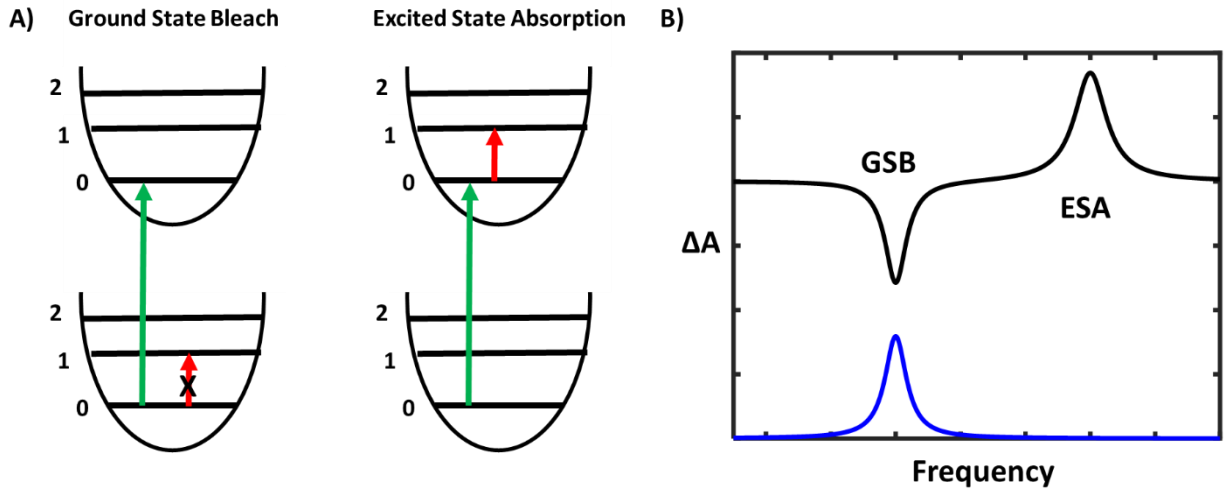

Figure 2-1: A) Representation of the transitions which give rise to both a ground state bleach (left) and excited state absorption (right) in which the green arrow represents the pump pulse and the red arrow represents the state observed by the probe beam. **B)** Example of the type of spectra typically obtained from TRIR with a ground state bleach and excited state absorption both present. The blue trace is the ground state absorption spectrum.

new species has been formed, with a different vibrational frequency, then a new signal with a positive amplitude will arise. This type of signal is termed an excited state absorption (ESA).[47, 50] **Figure 2-1** depicts the transitions described and their resulting spectra.

Shown in **Figure 2-2** below is a schematic representation of the TRIR setup used. In the case of our setup a frequency doubled Nd:YAG laser outputting 532 nm and operated at 15 kHz, while being chopped at 7.5 kHz, is used as the pump source. In order to allow for control of the energy density of the pump, a filter wheel with various neutral density filters is used. A ceramic globar, which produces continuous wave broadband mid-IR light in the 1000-4500 cm^{-1} range, is used as the probe source. The pump and probe sources are overlapped at the sample compartment, with the probe being focused through a monochromator and onto a mercury cadmium telluride (MCT) detector. The MCT detector is connected to an oscilloscope (Picoscope) which interfaces with a computer. The computer runs a custom MATLAB program that allows for control of the instrument and data collection.

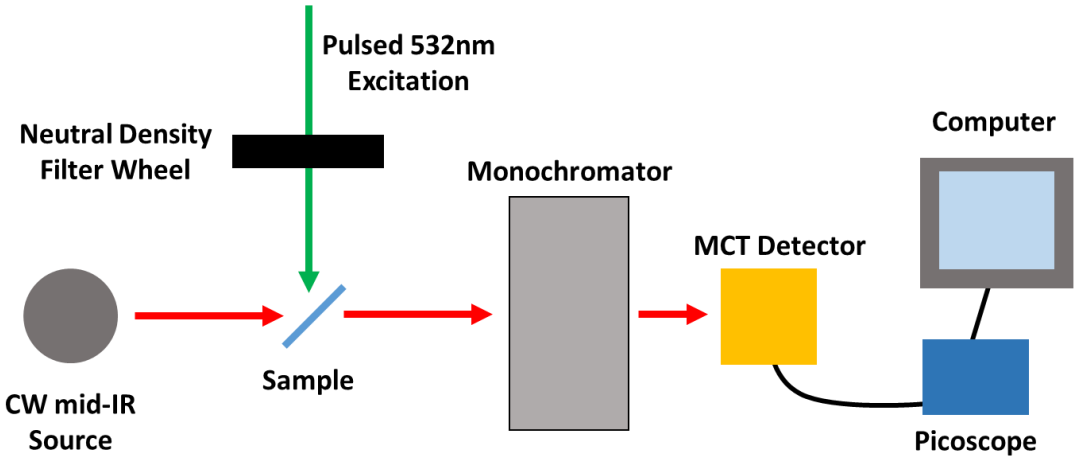

Figure 2-2: Schematic representation of nanosecond TRIR setup.

Photoluminescence Spectroscopy

To obtain information on the luminescent states of our material, a custom built photoluminescence setup was used, which is represented schematically in **Figure 2-3**. The excitation source is the same frequency doubled Nd:YAG laser outputting 532 nm at 15kHz and chopped at 7.5kHz, which used the same neutral density filter wheel to control the energy density of the beam mentioned previously. A monochromator is setup 90° relative to the excitation beam, with a lens between it and the sample to focus the light emitted by the sample. After the monochromator are a variety of photodiodes, which allow for collection of different parts of the ultraviolet and visible spectrum. These detectors are connected to an oscilloscope (Picoscope), which interface with a computer to control the instrument and collect data.

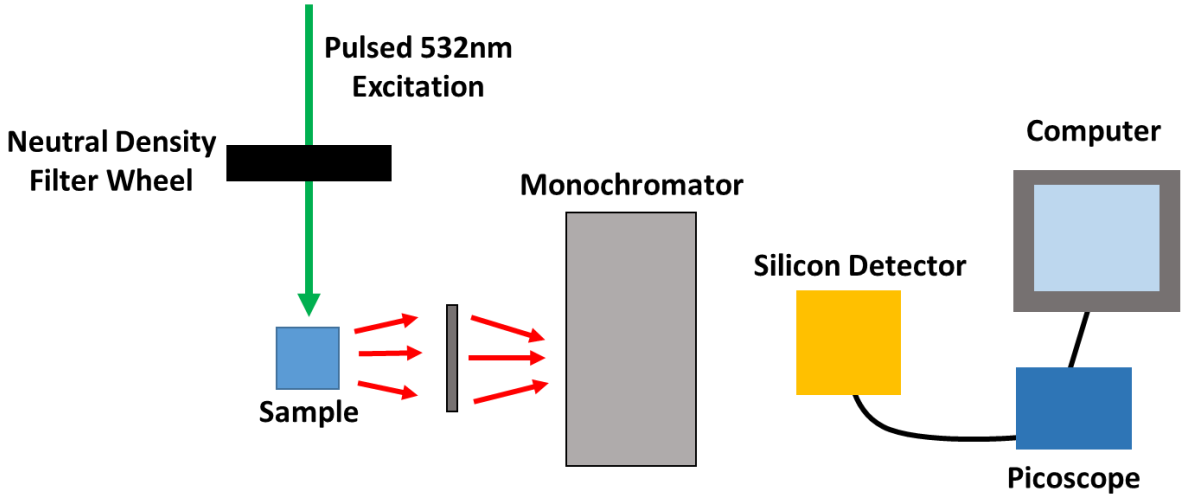

Figure 2-3: Schematic representation of nanosecond photoluminescence setup.

Chapter 3: Spectroscopic Line Shapes

Since a major component of the research in this thesis is focused on the interpretation of spectroscopic line shapes, this chapter is devoted to the basics of why specific line shapes are observed. This chapter also discusses a unique line shape known as a Fano resonance. The Fano resonance is a complicated line shape, which can arise in systems that have a discrete state which is degenerate in energy with a continuum of states. A more detailed description of the Fano resonance is provided below.

Basics of Line Shapes

If one were to imagine the electronic energy levels of a single atom, very well defined and discrete states would be observed, as shown in **Figure 3-1A**.[51] If the absorption spectrum of the atom was taken, then a single sharp peak would be detected for each transition that occurred (**Figure 3-1A**).[51] If we expand our view and begin looking at small molecules, then we see a change in the electronic states.[51] Unlike in the case of the atom, were each state was well defined, the molecule will have electronic states which are comprised of a number of substates. These substates are usually vibrational or rotational modes, as depicted in **Figure 3-1B**.[51] Thus, if an absorption spectrum of the molecule was taken then it would be comprised of a set of very closely

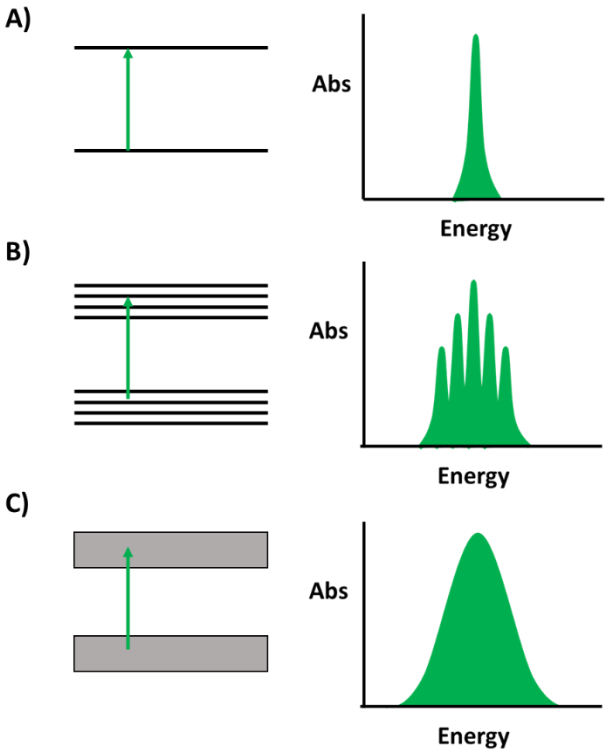

Figure 3-1: A) Atomic electronic states (left) with corresponding absorption spectrum (right). **B)** Small molecule electronic states (left) with corresponding absorption spectrum (right). **C)** Band electronic states (left) and corresponding absorption spectrum (right).

spaced peaks, which could be partially resolved (**Figure 3-1B**).[51] The molecule doesn't have well defined electronic states like the atom, due to the fact that to describe these states the motions of the atoms relative to one another must be accounted for.[51] These poorly defined states arise since there are multiple nuclear configurations which may correspond to the initial and final states of the system.[51]

Finally, if we go one step further and consider a network of covalently bonded atoms, such as for silicon, we see that the electronic states are comprised of unresolvable sub-states, which are often termed bands, shown above as **Figure 3-1C**.[52] The absorption spectrum of this network would appear as a broad featureless peak, which is due in part to accounting for the motion of the atoms, but also due to the Pauli Exclusion Principle.[52] The Pauli Exclusion Principle states that no two fermions can occupy the same quantum state, thus when the valence electrons of silicon form bonds with one another an energetic splitting occurs.[52] As more silicon atoms are incorporated the energies split, until they are no longer discrete and a band is formed, as depicted in **Figure 3-2**.[52]

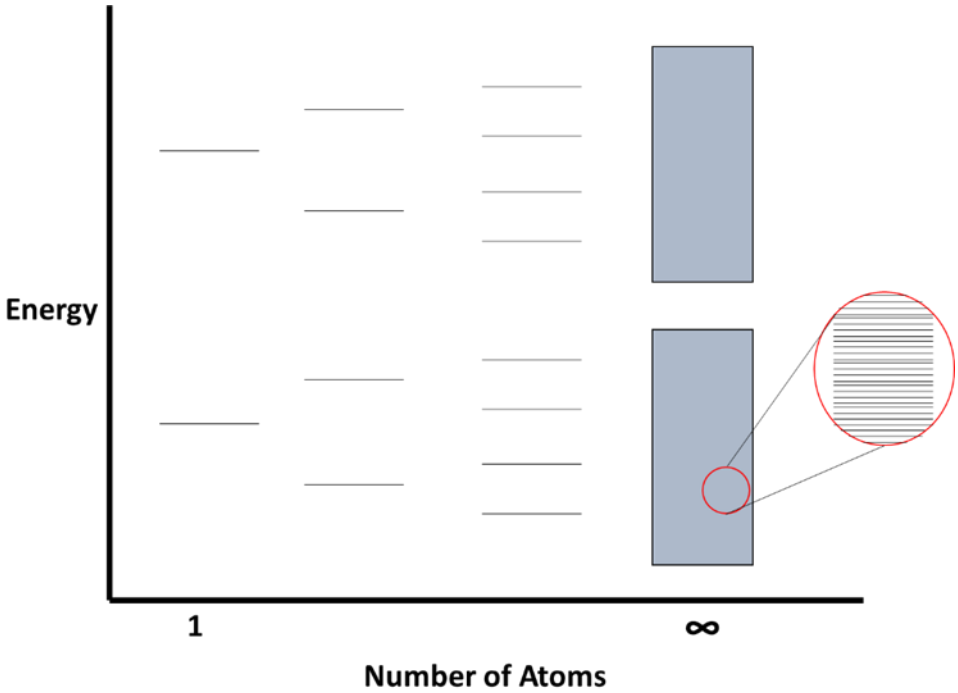

Figure 3-2: Depiction of the evolution of bands starting with a single atom, up to an infinite number of atoms covalently bonded together. Red circle is meant to represent a zoomed in view of the band showing that the band is comprised of a large number of states which are separated by an unresolvable energy difference.

Another mechanism which determines peak width is known as lifetime broadening, which is influenced by the excited state lifetime of the system.[52-53] If we imagine a simple two state system with a ground state and excited state, denoted m and n respectively, separated by some energy, E, as shown in **Figure 3-3A**. One could imagine exciting an electron from the ground state to the excited state using a photon with the appropriate energy.[52-53] It might be expected that if an absorbance spectrum was taken of this system, that one would expect to obtain a spectrum which looks like that depicted in F**igure 3-3B**, in which an infinitely sharp line is produced. However, instead something more akin to the spectrum in **Figure 3-3C** would be observed, in which a peak with a definite width is obtained.[52-53]

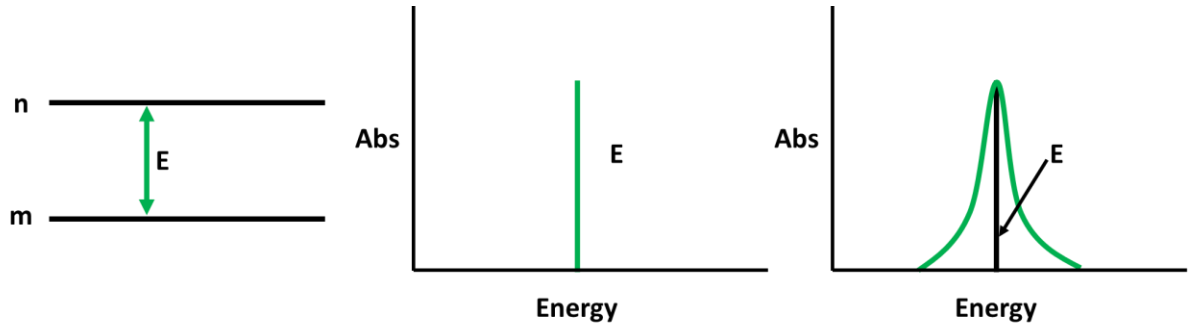

Figure 3-3: A) Simple two state system with an energy separation, E, between the ground state ,m, and excited state, n. **B)** Expected absorption spectrum based on system presented in 3-1A. **C)** Obtained absorption spectrum based on system 3-1A.

In order to understand why **Figure 3-3C** is produced, it is important to remember that an excited state has a finite lifetime, this is because it is energetically more favorable for the molecule to be in the ground state.[52-53] The decay process from the excited to ground state is a first order process and can be expressed as equation 3-1.[53]

$$-\frac{dN_n}{dt} = kN_n \qquad (3\text{-}1)$$

Where k is the first order rate constant and N_n represents the population of the n state.[53] By the Heisenberg uncertainty principle, given by equation 3-2, the product of the uncertainty in energy (ΔE) and the lifetime (t) must be greater than or equal to $h/4\pi$.[52-53]

$$t\Delta E \geq \frac{h}{4\pi} \qquad (3\text{-}2)$$

This means that tΔE must be greater than a predefined number, and thus informs us that the lifetime of the state is inversely proportional to the uncertainty of its energy. Thus, the longer lived a state is, the more well defined its energy, and since the rate constant of equation 3-1 has units of inverse time, it means that the rate of decay of a state is proportional to the uncertainty in its energy. This form of broadening is known as lifetime broadening, however it is rarely the sole source of linewidth broadening in a system.[52-53]

Another mechanism of line width broadening is dephasing.[54-55] When a system is initially excited, all of the oscillators are being driven such that they are in phase.[54-55] However over time the phase of the oscillators can change due to other interactions, such as elastic collisions.[54-55] As time progresses and more oscillators have a change in phase they begin to destructively interfere, doing so causes the coherence of the system to decay. The faster this dephasing time is the broader the peak becomes.[54-55]

The final mechanism which can lead to line width broadening is heterogeneity of the system.[53, 56] This form of line broadening is due to the differences in environment that each of the oscillators can experience.[53, 56] This can occur, for example, in a system which has multiple packing arrangements or crystal phases present at one time.[53, 56] These differences in local environment lead to a distribution of frequencies, which all correspond to the same species and because of this there is an observed line width broadening.[53, 56]

Fano Resonance

The Fano resonance was devised by its name sake, Ugo Fano, in 1961 as a way to explain the unique asymmetric line shape obtained from a study investigating the autoionizing states of atoms.[57-59] In order to account for this asymmetry Fano created an expression which took into

account the coupling of a discrete state which is degenerate with a continuum of states.[57-59] This can be seen below as equation 3-3.[57-59]

$$I = \frac{(q\gamma + w - w_0)^2}{(w - w_0)^2 + \gamma^2} \qquad (3\text{-}3)$$

Where q is the Fano parameter, w_o is the position of the resonance, and γ is the width of the resonance.[57-58, 60] Another formalism for this equation is shown below as equation 3-4. Where q is the Fano parameter and ε can be defined as equation 3-5.[57-58, 60]

$$I = \frac{(\varepsilon + q)^2}{\varepsilon^2 + 1} \qquad (3\text{-}4)$$

$$\varepsilon = \frac{2(w - w_0)}{\gamma} \qquad (3\text{-}5)$$

This equation was able to account for the asymmetric nature of the resonance obtained from the autoionization experiment.[57-58]

While the Fano equation was initially developed to fit data obtained from autoionization experiments, it has since been used throughout chemistry and physics to explain unique interferences in plasmonic, two-dimensional, and photonic materials.[58, 61-64] With Fano resonances becoming more prevalent in material systems, it is important to have an in-depth understanding of the phenomenon which gives rise to them.

It is useful to develop an understanding of what a resonance is before investigating the Fano resonance. All matter persist at some frequency when not being acted on by an external force, known as its natural or resonant frequency.[58] One example to consider would be the vibrational mode of a molecule, which we could approximate as a simple harmonic oscillator, such as in

Figure 3-4A.[65-66] It is important to remember that when the molecule is not acted on by an external force, the vibration will persist at its resonant frequency.[65-66] Resonance occurs when an external force is applied to the system and the frequency of this force is close to the resonant frequency of

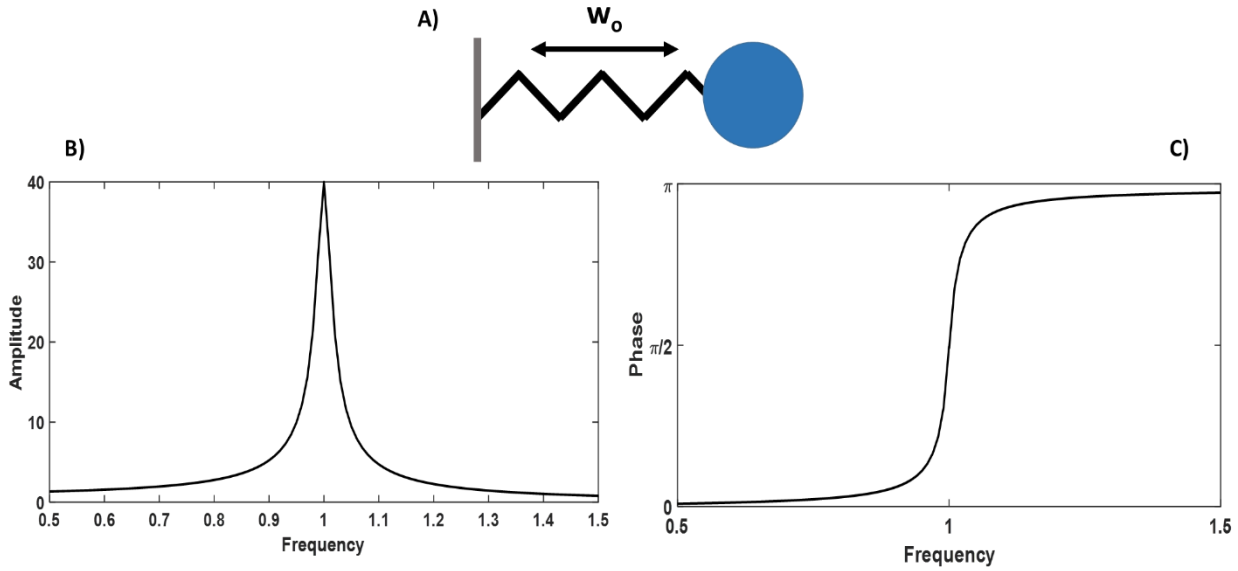

Figure 3-4: A) Depiction of simple harmonic oscillator with w_o representing its natural frequency. **B)** Plot of the amplitude of the harmonic oscillators oscillation as a function of the applied force with the resonant frequency of the harmonic oscillator being equal to 1. **C)** Plot of phase of the harmonic oscillator as a function of the applied force.

the oscillator.[65-66] At this point the amplitude of the resonant frequency is increased, due to being driven by the external force, shown as **Figure 3-4B** below.[65-66] Another important property of resonance has to do with the phase of the oscillation as the external force is applied.[65-66] Starting with the frequency of the external force at a value lower than the resonance frequency, and with both the external force and harmonic oscillator at a phase of zero, while initially increasing the frequency of the external force would cause the harmonic oscillator and external force to stay in phase, upon approaching the resonant frequency the phase of the oscillation would begin to shift, until attaining a value of $\pi/2$ at the resonant frequency, and later a value of π after the resonant frequency, shown below as **Figure 3-4C**.[65-66] Once the oscillator has achieved a phase shift of π, it will be 180° out of phase with the external force, meaning that the force being applied is actually acting in a destructive manner to the amplitude of the oscillation.[65-66] However, there are special

cases were the system has to be treated like two coupled harmonic oscillators, which can lead to asymmetric line shapes, as in the case of the Fano resonance.[59, 65-66] A perfect example of this is the enhanced signal one sees from the vibrational mode of a molecule deposited on a gold substrate, which is the basis of surface enhanced infrared spectroscopy.[61, 67-70]

As mentioned above, for a Fano resonance to arise there must be a discrete transition which is degenerate in energy with a continuum transition.[57-58, 62] Using equation 3-3 or 3-4 above allows for the fitting of a Fano resonance.[57-58, 62] The q parameter in the fit is unique to the Fano equation and is known as the Fano parameter, it controls the asymmetry of the fit.[57-58, 62] The Fano parameter represents a ratio of the transition amplitude of the discrete state to that of the continuum state, and is also related to the phase shift that the continuum undergoes. **Figure 3-5** depicts a number of Fano fits with varying q values.[57-58, 62, 71] While equations 3-3 and 3-4 can be used to fit the resonance, they don't give much information about the transitions leading to its creation. Luckily equation 3-4 can be expanded into 3 separate equations, with each part of the equation representing the discrete state, mixing, and continuum, which can be seen as **Figure 3-6**.[58, 62] In doing so one can theoretically extract out the pure line shape of the discrete transition.[58, 62]

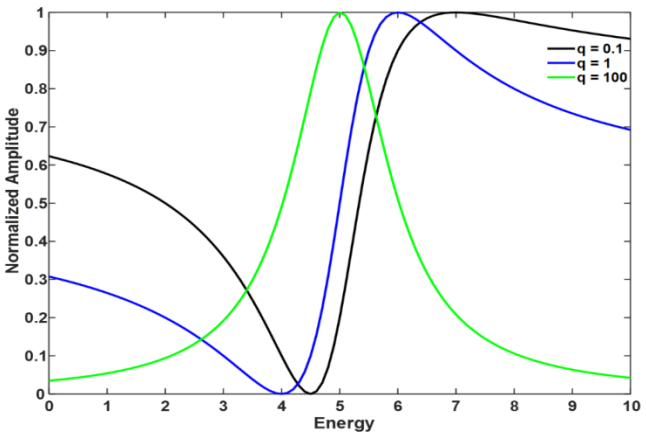

Figure 3-5: Fano equations with the discrete transition present at 5 and with varying q values. Notice how at q = 100 the lorentzian line shape is obtained.

As shown in both **Figure 3-5** and **3-6** the Fano resonance is asymmetric in nature, Which arises from the mixing of the discrete state and continuum, and their influence on the overall phase of the coupled system, relative to the external driving force.[57-58, 62] The Fano resonance can be explained using a model comprised of two harmonic oscillators, which both have different resonant frequencies, and are coupled together, as shown in **Figure 3-7A**.[65-66] For example, if the coupling constant between the two oscillators is 0, then the system can be treated like two single harmonic oscillators, except now there would be two peaks to represent the two different resonant frequencies.[65-66] This is because the harmonic oscillators are able to act independently and do not influence each other's motion.[65-66] However, if the coupling constant has a non-zero value, then the motion of one harmonic oscillator will influence the motion of the other.[65-66] We can model our system as one lower frequency harmonic oscillator (which would represent the continuum) and one higher frequency harmonic oscillator (which would represent the discrete state), as seen in **Figure 3-7A** below.[65-66] Applying a changing external driving force (which would represent the light used to probe the transitions) and tracking the amplitude of the system would lead to a peak, which would have a maximum value close to the resonant frequency of the lower frequency harmonic oscillator (continuum).[65-66] As the frequency of the external force (light) increases past the maximum value of the first peak (the continuum transition), the amplitude would decrease, until it reached a value of zero (typically denoted as the zero frequency).[65-66] The zero frequency

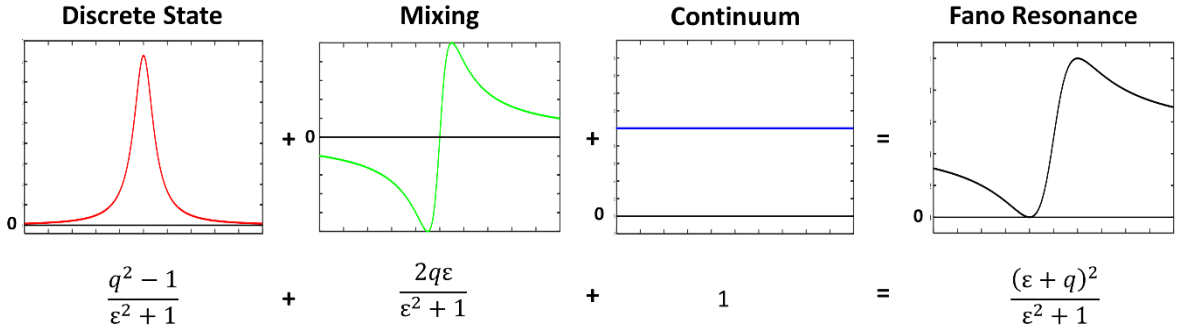

Figure 3-6: Fano equation separated into the components representing its discrete state, mixing, and continuum.

is at a lower value than the resonant frequency of the higher frequency harmonic oscillator (discrete state transition).[58, 65-66] As the frequency of the external driving force (light) increases past the zero frequency point, the amplitude of the oscillation would increase and peak at a value near the resonant frequency of the high frequency harmonic oscillator (discrete state transition), as shown in **Figure 3-7B**.[65-66] To obtain an understanding of why this occurs the phase of the lower energy harmonic oscillator (continuum) must be looked at as a function of the frequency of the external force (light).[57, 65-66] If we start with the external force (light) and lower frequency harmonic oscillator (continuum) both at a phase of 0, they will remain in phase until the frequency of the external force (light) begins to match the resonant frequency of the lower frequency harmonic oscillator (continuum), at which point there will be a phase shift to $\pi/2$.[65-66] Then, as the external driving force (light) increases past the lower frequency harmonic oscillators (continuum) resonant frequency, the phase would reach a value of π.[65-66] When the frequency of the external driving force (light) matches the zero frequency the phase would immediately drop to zero. This phase

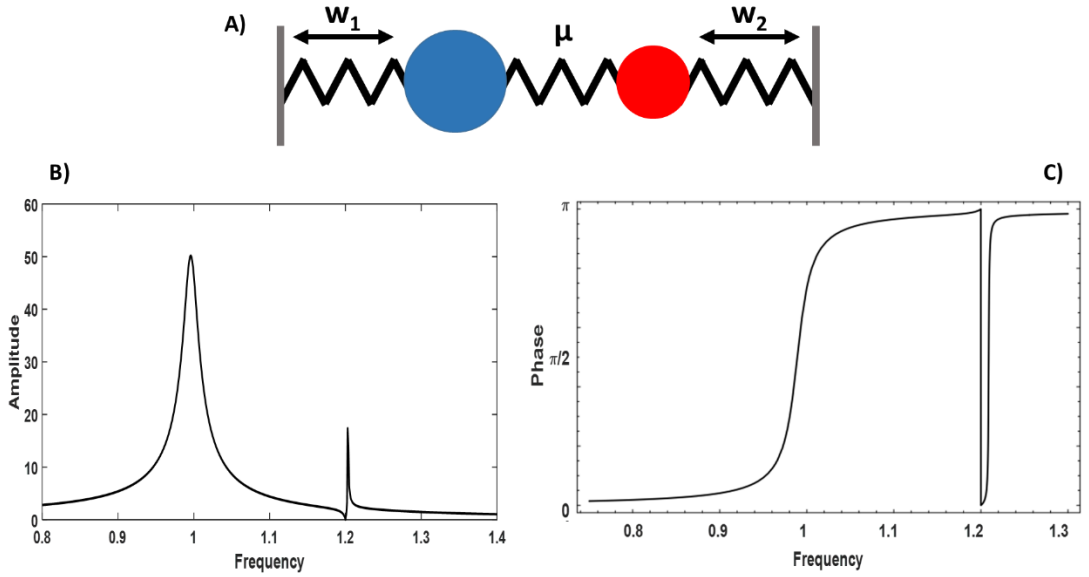

Figure 3-7: A) Depiction of classical model used to rationalize Fano resonances with w_1 and w_2 representing the resonant frequencies of the lower energy and higher energy harmonic oscillators respectively, and μ representing the coupling parameter. **B)** Plot of the amplitude of the lower frequency harmonic oscillator vs frequency of the driving force with resonant frequencies of 1 and 1.2 for w_1 and w_2 respectively. **C)** Plot of the phase of the lower energy harmonic oscillator vs frequency of the driving force. Adapted from reference 63.

shift is because the external force (light) is now beginning to influence the higher energy harmonic oscillator (discrete state) which has a phase of zero. The opposing phases of the two oscillators (the continuum and discrete state transition) cause their amplitudes to cancel and leads to the zero frequency.[65-66] As the external driving force (light) continues and passes through the higher energy harmonic oscillator (continuum), the phase increases to $\pi/2$ at the resonant frequency, and finally to π after it passes it, this phenomenon is depicted as **Figure 3-7C** above.[65-66] It is the coupling of the two oscillators and their unique phase relation which leads to the asymmetric character of the Fano resonance.[58, 60, 65-66]

The basics of line shape broadening and Fano resonances will be used extensively in Chapter 4. The Fano resonance is used in Chapter 4 in order to fit a set of TRIR spectra and extract the transient vibrational peak. The transient vibrational peaks obtained are then analyzed in terms of their center frequency and line widths.

Chapter 4: Analysis of $FAPbBr_3$'s Photophysical Properties Using TRIR

This chapter focuses on the analysis of the photophysical properties of $FAPbBr_3$ perovskite thin films. This study was inspired by previous work carried out in our lab, which sought to investigate the long lived charge-carrier lifetimes in $MAPbI_3$.[37-38] It was discovered through the use of TRIR spectroscopy that charge carriers in $MAPbI_3$ exist as large polarons, which are formed due to the interactions of the charge carriers with the phonon modes of the inorganic lattice.[37-38] On the basis of our previous work we were motivated to study FA^+ containing perovskites, due to their improved stability and complementary bandgap to $MAPbI_3$.[41, 72] We were also interested in whether the prior observations of polarons leading to long lifetimes in $MAPbI_3$ was a general property of halide perovskites, or specific to the iodide system.[37-38]

For example it has been observed that $FAPbBr_3$ single crystals exhibit longer charge carrier lifetimes than $MAPbBr_3$.[41] With some researchers speculating that the size of FA^+ limits its rotational freedom.[72-73] Allowing FA^+ to create more efficient polar domains, despite its smaller dipole moment than MA^+, which in turn allows for more efficient shielding of charge carriers.[27] Unfortunately, $FAPbI_3$ forms a photoinactive yellow phase upon synthesis, preventing us from making a direct comparison between $MAPbI_3$ and $FAPbI_3$ perovskite films.[26, 74] Conversely, both $FAPbBr_3$ and $MAPbBr_3$ variants form stable perovskite phases, enabling us to characterize how the organic cation affects charge carrier dynamics in halide perovskites.[18]

To better understand the electronic states of our material, we measured the absorbance and steady state PL spectra of a $FAPbBr_3$ thin film. **Figure 4-1** shows both the absorbance and steady state PL spectra of the perovskite film. In the absorption spectrum the shoulder located at ~530 nm has been attributed to excitonic absorption, and the continuously increasing absorption at shorter

wavelength is due to excitation to a continuum of states in the conduction band. [75-77] The photoluminescence spectrum has a single peak with a maximum at 548 nm. Due to the small Stokes shift between the absorption and photoluminescence spectra, it can be inferred that $FAPbBr_3$ emits from band edge states.[78]

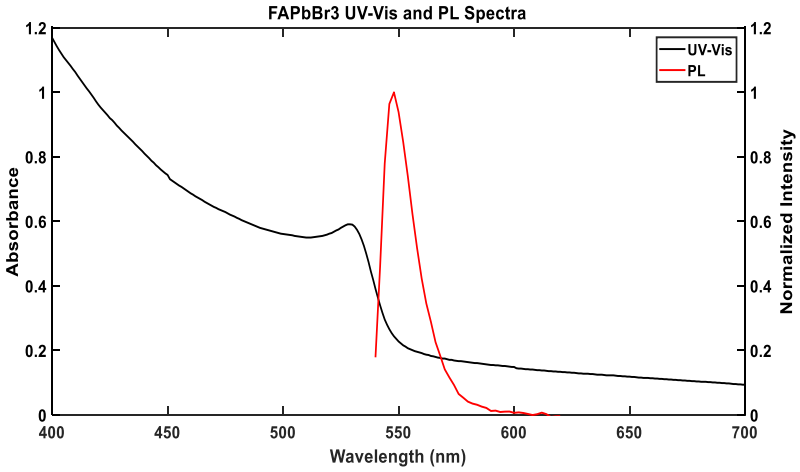

Figure 4-1: Absorption (black) and normalized photoluminescence (red) spectrum of $FAPbBr_3$ thin film.

To investigate the influence that electron-phonon coupling has on the band-edge states of $FAPbBr_3$, we performed temperature dependent PL spectroscopy. The PL spectra displayed (**Figure 4-2**) show that the emission intensity increases as the temperature is decreased. Indicating that fewer non-radiative decay pathways are present at lower temperatures, and thus leads to an increased PL quantum yield.[37, 79] The observation of a higher PL intensity at lower temperatures may be due to inefficient charge trapping or decreased electron-phonon coupling.[37, 76, 79] Interestingly, as the temperature is decreased, the peak maximum red shifts until 130K, at which point the peak suddenly blue shifts, followed by a continued red shift of the subsequent peaks. The red shift of the PL peak as temperature decreases has been attributed to

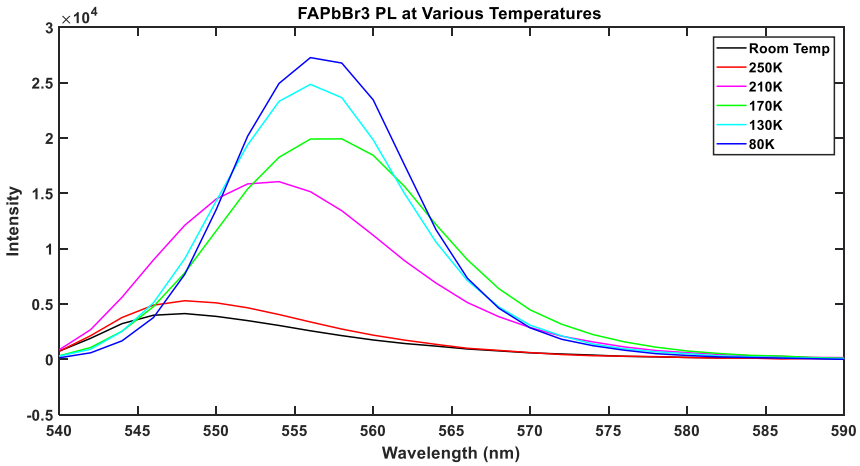

Figure 4-2: $FAPbBr_3$ photoluminescence spectrum at various temperatures.

contraction of the lattice, which increases the overlap of the Pb^{2+} 6s and Br^{-} 4P orbitals comprising the valence band, and decreases the band gap.[18, 26] The sudden blue shift at 130 K has also been attributed to a change in orbital overlap caused by a phase change.[80]

Unlike the more commonly studied $MAPbI_3$, whose phase transitions have been well documented, there is not a general consensus regarding the phase transitions of $FAPbBr_3$.[16, 77, 81-83] However, because of the abrupt blue-shift observed in the temperature-dependent PL spectra around ~130 K, we speculate that $FAPbBr_3$ undergoes a phase transition at ~130K.[80] Therefore, we decided to compare the data collected at room temperature and 170 K, to avoid possible discrepancies due to a phase change.

To aid in our understanding of the $FAPbBr_3$ photophysics, TRIR spectroscopy was carried out at both room temperature and 170K. **Figure 4-3** shows TRIR spectra collected at room temperature and 170 K following optical excitation at 532 nm. Previously, our lab has shown that even at temperatures as low as 150 K the majority (>80%) of excitons produced are able to dissociate, due to their low binding energy (~10 meV).[37-38] Also, the majority of free carrier

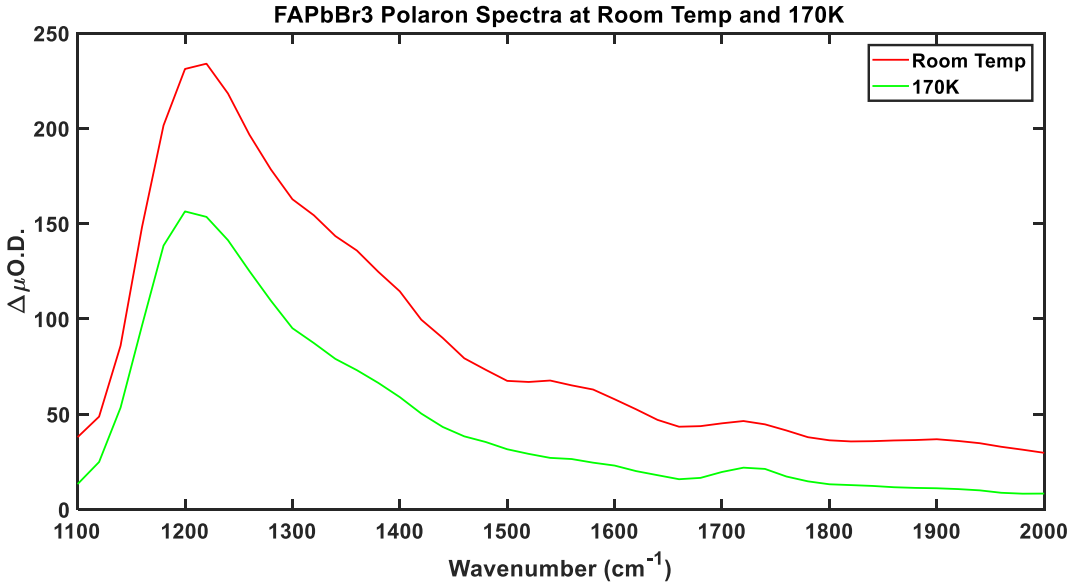

Figure 4-3: $FAPbBr_3$ TRIR Spectra collected at Room temperature and 170K.

absorption is centered in the lower frequency range of the spectrum.[37] So we do not expect a major contribution of our transient signal to arise from either excitons or free carriers. Thus, we assign the signal to the photoionization of large polarons. As shown by **Figure 4-3**, going from room temperature to 170 K leads to a ~50% decrease in the transient signal intensity. This suggest that while the electron-phonon interactions of $FAPbBr_3$ do vary with temperature, they do not vary to the same degree as in $MAPbI_3$, which showed a factor of 4 change in the polaron spectrum over a similar temperature range.[37-38]

The importance of electron-phonon coupling in halide perovskites has been shown by a temperature-dependent photoluminescence study performed by Herz et al..[76] The study determined that the primary interaction charge carriers experience is scattering with longitudinal optical (LO) phonons.[76] To ascertain how the changes in electron-phonon coupling were affecting the formation of large polarons, we fit our normalized TRIR spectra with the large polaron model created by Emin (equation 1-3).[35] As described in Chapter 1, the large polaron model treats the photoionization of a polaron as a hydrogenic model.[35] With the absorption maximum occurring at

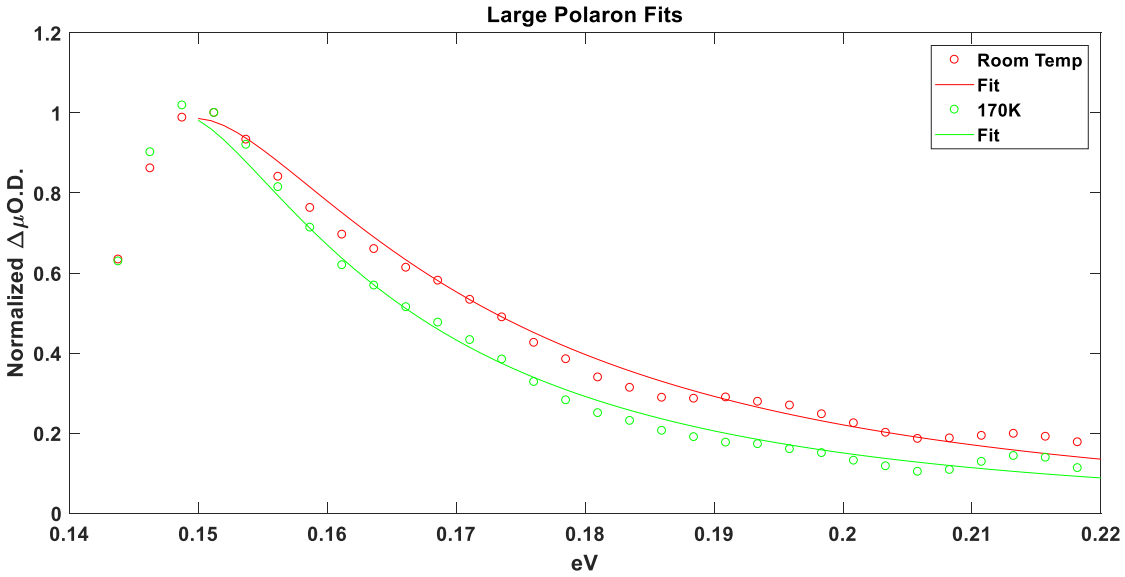

Figure 4-4: $FAPbBr_3$ TRIR spectra collected at room temperature and 170K with large polaron fits overlaid.

three times the polaron binding energy.[35] In the case of $FAPbBr_3$, the peak maximum occurring at ~1200 cm^{-1} results in a polaron binding energy of ~0.05 eV, very similar to that of $MAPbI_3$ measured previously.[35] For the fit, we used a mass of $0.2m_e$, which had previously been adopted to calculate the recombination coefficients of $MAPbI_3$ and $MAPbBr_3$, and allowed the effective delocalization length to be varied to optimize the fit, shown as **Figure 4-4**.[84] The fits produced values of ~5 and ~6 nm for the effective delocalization lengths of room temperature and 170 K respectively. Previous work in our lab discovered that the delocalization length for $MAPbI_3$ was 9 and 13 nm at 150 and 310 K respectively.[37] It was observed that the increased delocalization at low temperature for $MAPbI_3$ was due to a decrease in the dynamic disorder and fluctuations of the inorganic lattice.[37] This explanation was supported by analysis of the transient vibrational dynamics of the N-H bend of MA^+.[37-38] It was found at room temperature there was a blue shift of the transient N-H bend by 10 cm^{-1}, relative to its ground state FTIR feature.[37-38] It had previously been discovered that the N-H bend of MA^+ was sensitive to hydrogen bonding with the inorganic lattice, with a blue shift in frequency corresponding to a weakening of the hydrogen bonding interaction.[39-40] Since the blue shift occurred in the transient spectra, it signified that in the presence of charge carriers the hydrogen bonding interactions with the inorganic lattice were weakened.[37] As the temperature decreased, the transient vibrational signal simultaneously red shifted and narrowed.[37] The increased blue shift at higher temperature implied a greater weakening of the hydrogen bonding interactions, which was due to an increased population of large polarons.[37] The increased peak breadth indicated there was a greater vibrational dephasing time, due to the larger amplitude and potentially higher frequency lattice fluctuations.[37-38]

As had been done previously in the $MAPbI_3$ study, we decided to investigate the transient vibrational dynamics of FA^+ in the presence of charge carriers, in order to better understand how

the vibrational dynamics of the lattice affect the optoelectronic properties of the material. As previously stated, the A site cations in halide perovskites do not contribute to the band edges of the material.[18] Because of this, FA^+ does not directly interact with our pump pulse, thus any changes in its vibrational modes will be due to changes in its local environment. **Figure 4-5** shows the ground state FTIR of $FAPbBr_3$ taken at room temperature. The vibrational feature centered at 1716 cm^{-1} has been identified in other work as the C-N asymmetric stretch.[85] Due to the relatively high oscillator strength of this vibration we reasoned it would make a good candidate for analysis in TRIR spectroscopy.

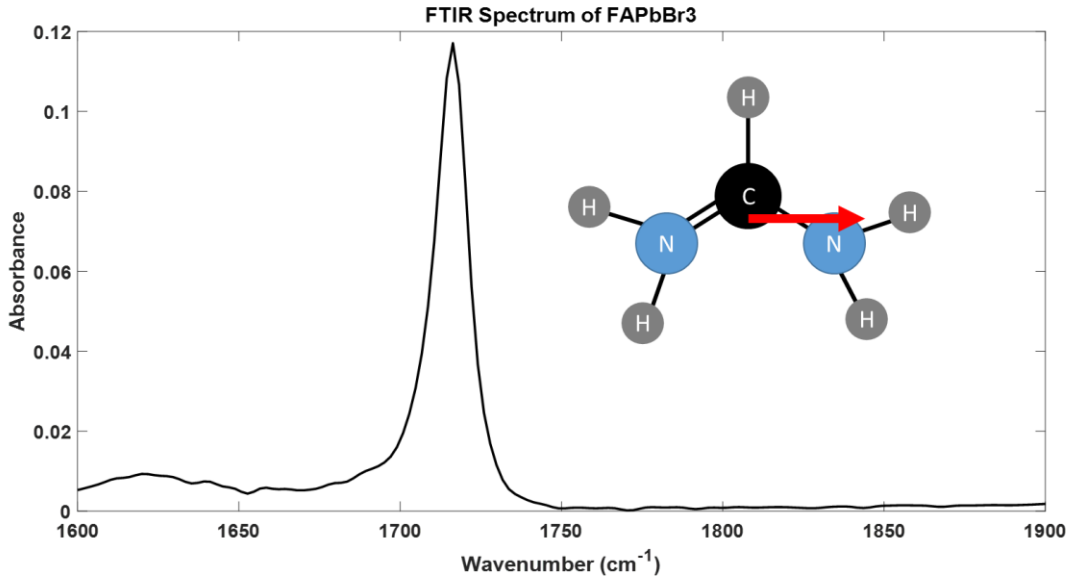

Figure 4-5: $FAPbBr_3$ FTIR Spectrum, inset figure shows formamidinium molecule and direction of dipole moment associated with vibrational transition.

Figure 4-6 shows the region of the TRIR spectrum where the transient C-N vibration arises. Since the vibration is superimposed onto the high frequency tail of the polaron, a third order polynomial was used to separate out the vibration to allow for its interpretation. The combination of the offset bleach and the unique asymmetry of the recovered spectrum forced us to rethink our initial interpretation of the data, and required us to look for a model which could capture all of its features. Below we have included our rational as to why our initial interpretation proved to be invalid, following which we discuss what led us to choose the new

model. Initial analysis of the signal obtained after subtraction lead us to believe that we had captured both the bleach of the C-N ground state, and the corresponding induced absorption**.** However, the location of the ground state bleach didn't match the location of the ground state vibration. That is, the peak maximum of the ground state vibration is at ~1716 cm^{-1}, while the minimum point of the bleach occurs at ~1705 cm^{-1} (**Figure 4-6**). The observation of a negative feature at 1705 cm^{-1} is inconsistent with the position of the ground state bleach, which should represent a reduction in the ground state vibration of C-N. The spectrum also shows an asymmetry to it, which makes fitting of the data difficult. This can be seen in both the bleach, which has a long low frequency tail, and in the induced absorption, which has a long high frequency tail. As mentioned above, due to these inconsistencies a different model had to be found to interpret the data.

Because of the large oscillator strength of the excited state vibration and the proximity to the polaron absorption, we reasoned that there was coupling between the vibrational mode of the organic cation and the polaron electronic state. This form of enhancement is similar to that which occurs between a surface plasmon resonance and a molecular vibration.[61, 67, 69] We attributed the asymmetric line shape of the transient vibration to a Fano resonance. Which we reasoned was due to coupling of the higher energy Drude-like absorption tail of the

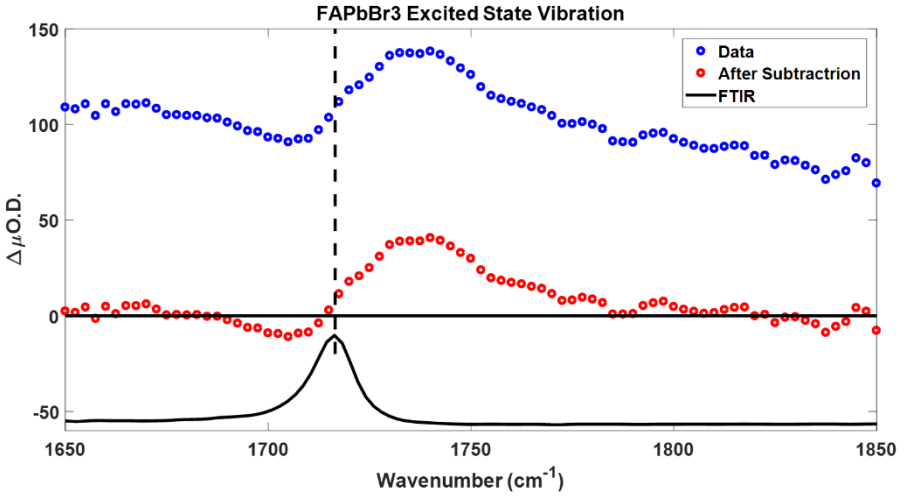

Figure 4-6: $FAPbBr_3$ Excited State C-N Vibration before and after subtraction of third order polynomial. Dashed line is a guide to the eye emphasizing displacement of the ground state vibration from the suspected bleach.

polaron, which arises from excitation of self-trapped carriers to a continuum band of states, and the discrete vibrational mode of the transient C-N vibration.[58, 62, 65] Thus, using a combination of the Fano equation and a third order polynomial, which served as a suitable approximation of the polaron absorption, we were able to adequately fit our data, which can be seen below as **Figure 4-7**.

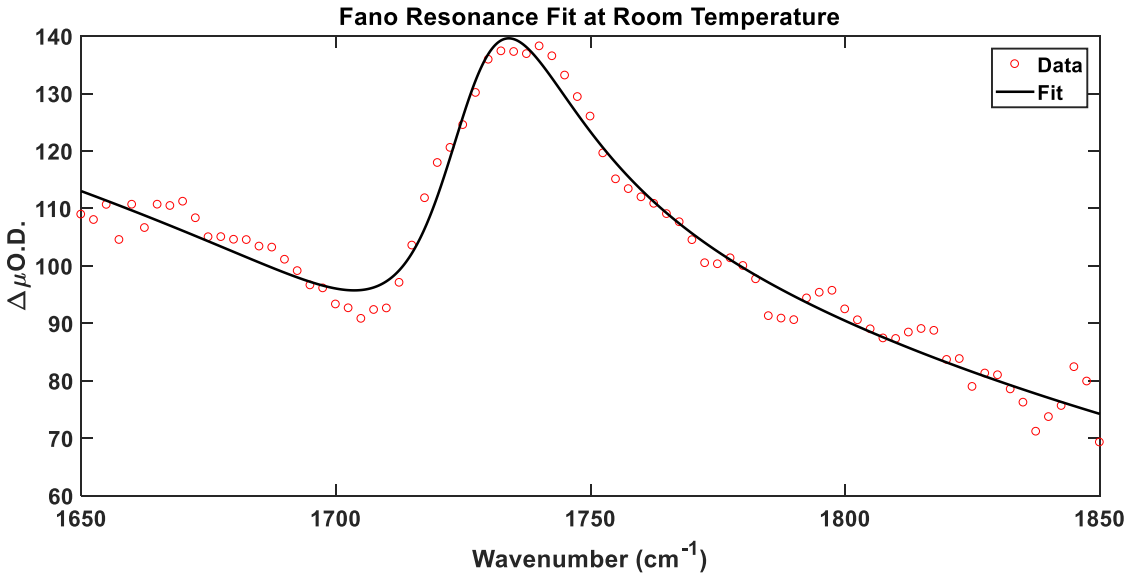

Figure 4-7: $FAPbBr_3$ excited state C-N vibration with third order polynomial and Fano resonance fit overlaid on top.

As mentioned in Chapter 3 the Fano equation is comprised of three separate components representing the discrete state, mixing, and continuum which give rise to the signal.[58] Decomposing the fit allowed us to extract and analyze the discrete state, representing the transient vibration, shown below as **Figure 4-8A** and **B** for the room temperature and 170K respectively. The vibrational peaks obtained from the decomposition of the Fano equation can be seen below in **Figure 4-9**. It was found that the center frequency of both peaks lie at 1727 cm^{-1} and the FWHM was 31.9 and 23.3 cm^{-1} for room temperature and 170K respectively.

It is useful to compare and contrast the transient vibrational spectra measured for FAPbBr3 with those measured for $MAPbI3_3$. The $MAPbI_3$ and $FAPbBr_3$ are both similar in it that as the temperature is decreased there is a decrease in the FWHM of the excited state vibration.[37-38] However, unlike in the case of the $MAPbI_3$ N-H bend, which showed a red shift in frequency as temperature was lowered, $FAPbBr_3$ keeps the same frequency at both temperatures. For $MAPbI_3$, the increase in FWHM with respect to temperature was explained as occurring due to the increase in dynamic disorder and fluctuations of the inorganic lattice.[37-38] This is because the FWHM of a vibration is inversely proportional to its dephasing time, which is a metric of how long the ensemble of vibrational modes in a sample keep their initial phase with respect to each other.[37-38, 86] Loss of this phase is due to a combination of vibrational relaxation, spectral diffusion, and elastic collisions with the inorganic lattice due to thermal fluctuations.[37-38, 86]

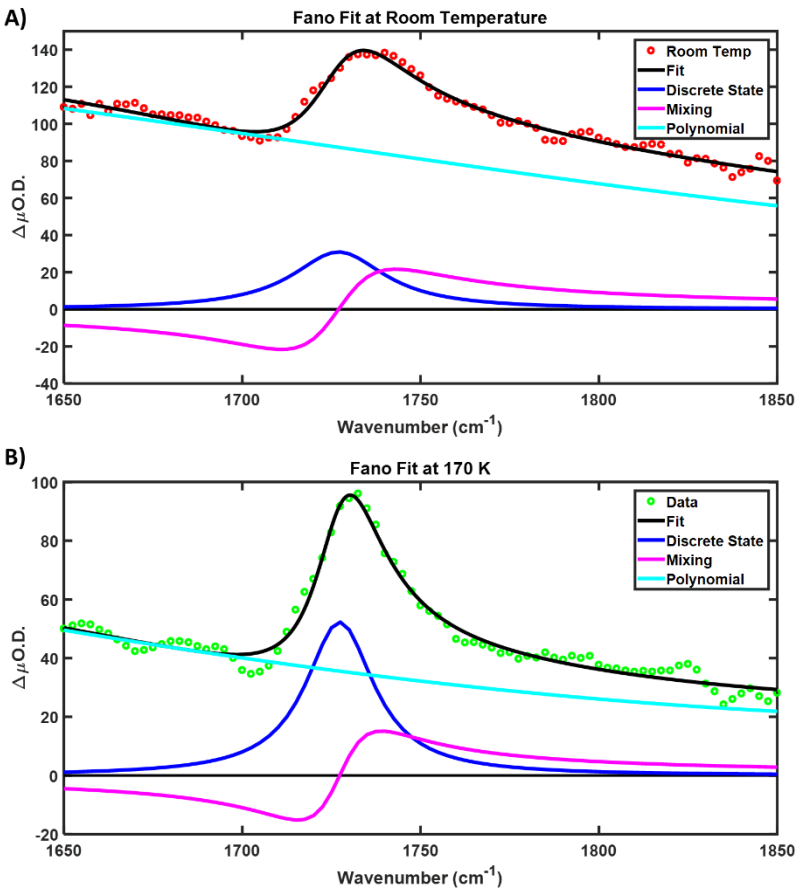

Figure 4-8: A) $FAPbBr_3$ room temperature and **B)** $FAPbBr_3$ 170K excited state C-N vibration and overlaid Fano fit with discrete, mixing, and polynomial functions obtained from decomposition, continuum excluded for clarity.

As the temperature of the sample is increased the number of times the A site cation can undergo elastic collisions with the inorganic lattice increases, and in doing so the vibrations of the cation have a chance to undergo a phase shift, which leads to the overall number of molecules persisting at the initial vibrational frequency and phase to decrease, as the molecules which are phase shifted begin to destructively interfere with the others.[38, 86] We believe that since the FWHM of the C-N stretch of $FAPbBr_3$ follows a similar pattern as $MAPbI_3$, that we are capturing the increased dynamic disorder of the inorganic lattice in the excited state. However, unlike in the case of the N-H bend for $MAPbI_3$, we do not see a shift in vibrational frequency of the C-N stretch of $FAPbBr_3$. For $MAPbI_3$ the reason that the vibration blue shifts at higher temperatures is due to the weakening of hydrogen bonding with the inorganic lattice.[37-40] Thus as the hydrogen bonding weakens the N-H bond becomes stronger and higher in energy.[37-40] In the case of the C-N stretch of $FAPbBr_3$, we believe that one of two scenarios is influencing its dynamics. The first is when considering the C-N stretch there is no hydrogen bonding occurring between the lattice and either the carbon or nitrogen. So, while the strength of the hydrogen bonds with the inorganic lattice might be changing, the atoms involved in the vibrational mode being probed are not involved in the interaction.

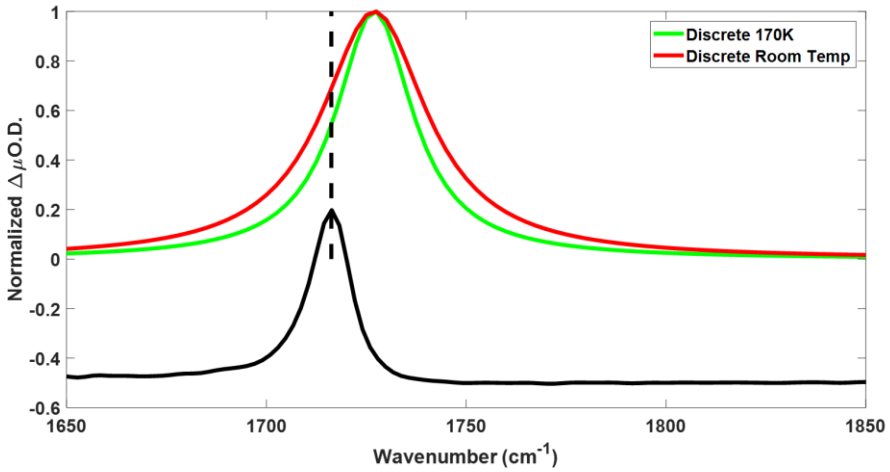

Figure 4-9: Comparison of excited state vibration extracted from the Fano fit of $FAPbBr_3$ at room temperature and 170K, along with the FTIR spectrum of the ground state vibration.

The second scenario we are considering could have to do with differences in the dynamics of the MA^+ and FA^+. Theoretical calculations have predicted that the dynamics of FA^+ and MA^+ show drastically different responses to temperature.[73, 82, 87] With FA^+ predicted to keep a similar degree of rotational freedom as temperature is lowered.[72-73, 77] However, the dynamics of MA^+ become severely retarded at lower temperature, with its tumbling motion being completely frozen out in its low temperature orthorhombic phase.[82, 87-88] This would imply that FA^+ experiences a similar environment at high and low temperature, potentially explaining the similar transient vibrational response, while the change for MA^+ is due to the more drastic differences in its rotational and vibrational dynamics. Either of these scenarios listed above could be the cause of the differences we observe in our TRIR spectroscopy measurements.

Our transient vibrational data demonstrates that at elevated temperatures, in the excited state, there is an increased dynamic disorder of the lattice, implying an increase in the electron-phonon coupling of the system. Electron-phonon coupling is a common mechanism by which radiative quenching can occur, as it increases the number of non-radiative decay pathways increases, as emphasized by **Figure 4-2,** which presented the decrease in PL quantum yield as temperature increased.[37, 79] Data from **Figure 4-3**, which presented an increase in the large polaron population at higher temperatures, suggest that for $FAPbBr_3$ the increased electron-phonon coupling leads to an increase in the probability of charge carriers becoming self-trapped as large polarons. Also, as evidenced by the delocalization lengths extracted from the polaron spectra, at higher temperature the polarons become more localized. This localization likely leads to decreased wavefunction overlap and contributes to the decreased radiative recombination probabilities, which in turn leads to the enhanced charge carrier lifetimes.

On the basis of this work, $FAPbBr_3$ has been shown to form large polarons with a similar binding energy as $MAPbI_3$. The large polarons of both materials have been found to localize more at higher temperature, which is due to the increased electron-phonon coupling present. The formation of large polarons is also the reason for the long charge carrier lifetimes in both films. However, it appears as though $FAPbBr_3$ is less impacted by dynamic disorder then $MAPbI_3$, as evidenced by the 50% decrease in polaron population going from room temperature to 170 K for $FAPbBr_3$, compared to the 4 fold decrease observed for $MAPbI_3$. It was also observed that the vibrational dynamics of the A site cations do not follow the same trend with temperature, with FA^+ showing no shift in vibrational frequency and MA^+ blue shifting at higher temperature.[37-38] Leading us to theorize that the dynamics of the A site cation and phonon modes of the lattice heavily influence one another. In Chapter 5 we propose a number of anisotropy and TRIR experiments, which we believe will help tease out why we saw differences in the transient vibrational modes probed, and whether they are due to the dynamics of the A site cation or the moieties measured.

Chapter 5: Future Directions

As shown previously in Chapter 4, our TRIR and PL data has suggested that the fluctuations of the inorganic lattice control the optoelectronic properties of lead halide perovskites. Specifically, our findings have shown that due to electron-phonon coupling, charge carriers in $FAPbBr_3$ are predominantly present as large polarons. Which leads to the increased localization of charge carriers and decreases their wavefunction overlap, producing the enhanced lifetime the material is known for.[37, 89] However, we also observed obvious differences in our TRIR spectrum for the C-N stretch of $FAPbBr_3$ and the N-H bend of $MAPbI_3$. With the center frequency of the transient C-N signal showing no change with temperature, while the transient signal of the N-H bend blue shifts as temperature was increased. Because the N-H bend mode is able to couple to the inorganic lattice through hydrogen bonding, changes in the mode occupancy of the lattice phonons will lead to changes in the hydrogen bonding strength, which in turn will lead to changes in the frequency of the N-H bend.[37-38] However, this same comparison cannot be made for the C-N stretch of $FAPbBr_3$, as we believe there could be two reasons for the lack of a shift in center frequency. The first would be that since the C-N moiety of FA^+ isn't able to hydrogen bond with the inorganic lattice, any distortions or changes in phonon mode occupancy would not lead to changes in the frequency of the C-N stretch. The second explanation could be that the changes to the FA^+ dynamics are subtle, and thus not reflected in our transient vibrational data.

Previously, several theoretical and experimental reports have investigated the dynamics of the organic cation. It has been proposed through molecular dynamics (MD) simulations that at

room temperature, MA^+ is able to rotate almost freely inside of the inorganic lattice.[73, 85, 88, 90-91] The two primary rotational modes predicted to exist for MA^+ are a wobbling motion about the C-N axis and a reorientational jump between adjacent faces of the lattice, represented in **Figure 5-1A**.[85, 91] With this modeling, and neutron scattering techniques, it has been proposed that at lower temperature (~100 K) the reorientational jump of MA^+ is completely frozen out, leaving only the wobbling motion active.[91] While less has been done on FA^+ it has also been proposed, through MD simulations, that there are two primary rotational modes it can undergo, which are similar to those of MA^+.[73, 85] The first mode is rotation about the axis produced by the two nitrogen atoms, and the second is a jump causing the two NH_2 groups to switch to adjacent faces of the inorganic lattice, depicted in **Figure 5-1B**.[73, 85] The two rotational modes of FA^+ have also been shown experimentally, through the use of room temperature 2D infrared (IR) anisotropy experiments, which shows two dynamic processes occurring on the ultrafast time scale. It has been predicted for FA^+ that both of its rotational modes stay active, even down at temperatures were the wobbling mode of MA^+ freezes out.[73, 85, 88] However to our knowledge no experimental data exist to confirm this.

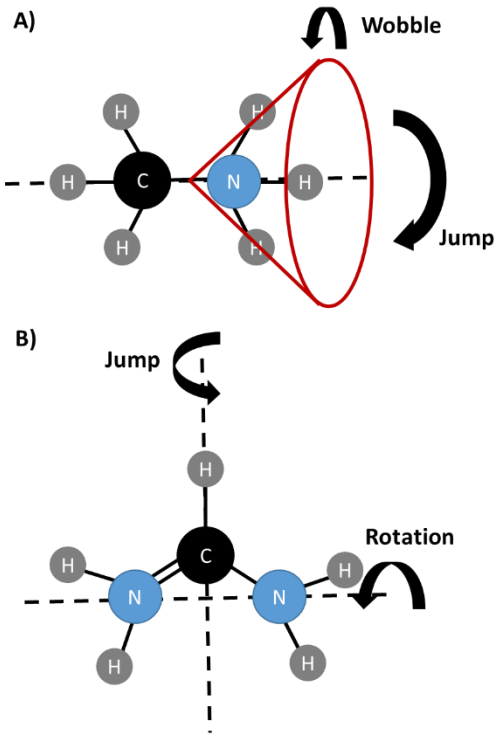

Figure 5-1: Rotational modes of **A)** MA^+ and **B)** FA^+.

As mentioned previously, while some work has been done to study the dynamics of the organic cations in lead halide perovskites, to our knowledge there has not been a comparative study of their dynamics as a function of temperature. As a result, we propose to measure infrared

orientational anisotropy decays of the C-N stretch of FA^+ in $FAPbBr_3$, and the N-H bend of MA^+ in $MAPbBr_3$ using polarization selective infrared pump-probe spectroscopy in both the ground and excited state. Additionally, we propose to use TRIR spectroscopy to measure the transient N-H stretch modes of $FAPbBr_3$. Since the N-H stretch mode can couple with the lattice via hydrogen bonding, it will be sensitive to changes in the phonon mode occupancy of the lattice, allowing us to provide further evidence as to whether or not $FAPbBr_3$ is undergoing drastic changes in lattice dynamics. The data collected will provide evidence for whether FA^+ is able to keep a similar rotational degree of freedom across various temperatures, as has been proposed by theory. We will also be able to make a direct comparison to the dynamics of MA^+, which will allow us to explain the differences we see in our TRIR data. As polarization selective IR pump-probe spectroscopy is able to measure the dynamics of the cation directly, we will be able to see if FA^+ has considerably different dynamics at lower temperature. Using both polarization selective IR pump-probe and TRIR spectroscopy will inform us as to whether the lack of shift in the TRIR spectrum is due to, insignificant changes in cation dynamics, or a lack of hydrogen bonding of the atoms involved in the C-N stretch with the lattice.

Polarization Selective IR Pump-Probe Spectroscopy

Using polarization selective IR pump-probe spectroscopy allows for the acquisition of both rotational lifetimes and orientational relaxation.[86, 92] Like other pump-probe methods, this

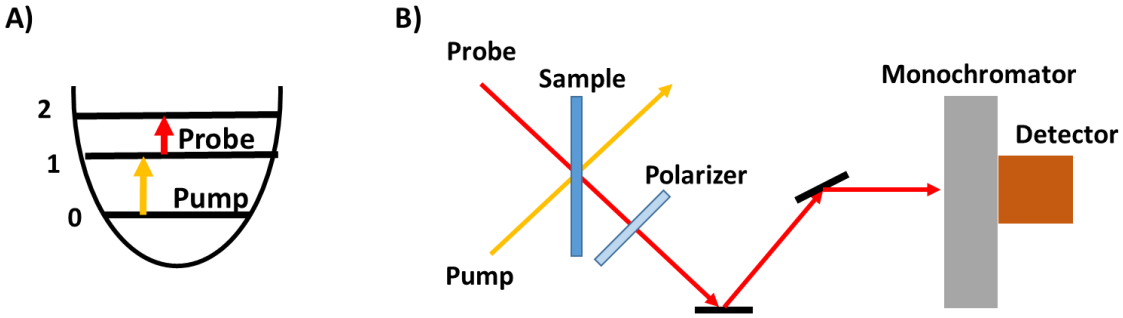

Figure 5-2: A) Energy level diagram depicting purpose of pump and probe pulses. **B)** Simplified polarization selective IR pump-probe setup.

technique involves the use of a pump pulse, used to create an excited state population, and a probe pulse, used to monitor the decay of the newly populated state.[85, 93] By delaying the pump and probe in time, dynamic information is able to be recovered about the system being studied.[94-95] In the case of polarization selective IR pump-probe spectroscopy, both the pump and probe lie in the infrared region of the electromagnetic spectrum and are used to promote the 0→1 and 1→2 vibrational transitions respectively (**Figure 5-2A)**.[93-95] **Figure 5-2B** depicts a simplified schematic of a typical polarization selective IR pump-probe setup. The pump and probe beams are produced by an ultrafast laser, typically with a pulse duration of ~100 fs.[93] The pump pulse is linearly polarized in one direction before exciting the sample, while the probe pulse is polarized 45° relative to the pump, insuring there is a parallel and perpendicular component with which to probe the sample.[95-96] Use of a computer controlled polarizer, placed after the sample, allows for selective measurement of the parallel and perpendicular components.[95-96]

In order to understand how polarization selective IR pump-probe spectroscopy works, it is useful to build up from how the polarization of light affects its interaction with matter. If one was to imagine a light source which was linearly polarized, like that depicted in **Figure 5-3**, the only way in which a molecule could interact with it would be if a projection of its dipole aligned with it.[96-99] In order to visualize this interaction, one can imagine an xy coordinate plane, set up in such a way that the y axis is parallel to the polarized lights electric field (E).[96-99] A molecule with a transition dipole moment (μ) in this coordinate plane will make an angle (θ) with the y-axis, as shown in **Figure 5-3**. The molecule will have the

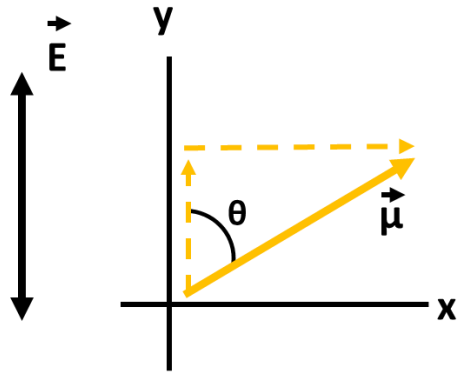

Figure 5-3: Depiction of linearly polarized light (E) along with a molecule with transition dipole moment (μ) at angle θ from x axis. Dashed lines represent the x and y projections of the dipole moment.

highest probability of interacting with the light when its transition dipole moment is positioned parallel to the electric field ($\theta = 0°$).[96-99] As the angle, θ, increases the probability of interacting with the electric field decreases.[96-99] This decrease is due to the projection of the dipole, which is parallel to the electric field, becoming smaller at higher values of θ.[96-99] This decrease will continue until $\theta = 90°$, at which point there will be no component of the dipole which can interact with the electric field.[96-99]

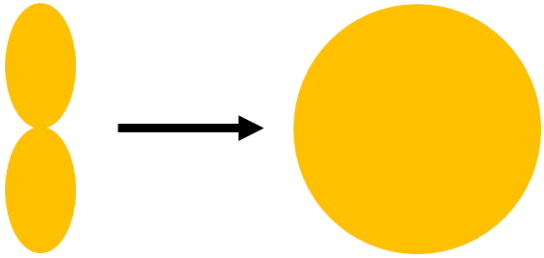

Figure 5-4: Depiction of a cos θ distribution of excited molecules will evolve into an isotropic distribution over time. Distributions are presented in polar coordinates.

Using the above concept, we can determine that a linearly polarized pump beam will lead to a cos θ distribution of excited molecules, as shown in **Figure 5-4**.[93, 96-97] Once the molecules have been excited there are two major processes they can undergo.[93, 96-97] First, the molecules can undergo vibrational relaxation, which leads to a decrease in the absorption signal of the probe regardless of its polarization.[93, 96-97] Additionally, the molecules can also rotate, and this rotation is a key component of the polarization selective IR pump-probe technique.[93, 96-97] As stated above, only molecules which have projections of their transition dipole moment parallel to the pump pulse will be excited, leading to a cos θ distribution.[96-99] Over time the molecules can

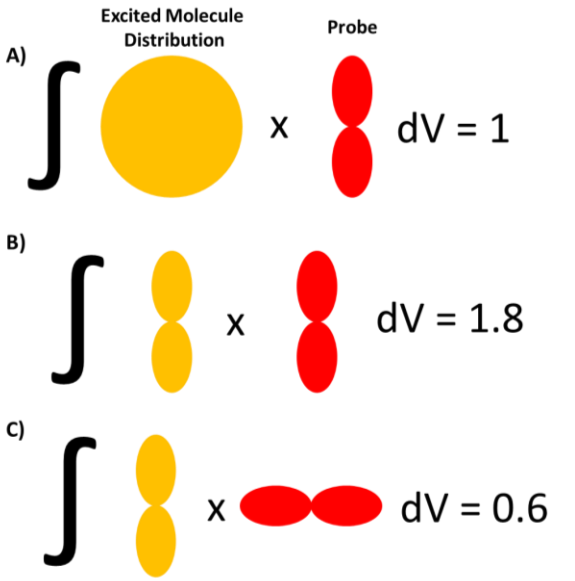

Figure 5-5: Overlap integral of **A)** isotropic distribution of excited molecules with distribution probed by linearly polarized pulse. **B)** cos θ distribution of excited molecules with distribution probed by parallel polarized beam. **C)** cos θ distribution of excited molecules with distribution probed by perpendicularly polarized beam.

either undergo vibrational relaxation or rotate. Eventually the molecules will have randomized their directions, meaning that there is now an isotropic distribution of excited molecules, shown as **Figure 5-4**.[96-99] This rotational evolution means that the signal we obtain from our probe will differ, depending on its polarization.

To better understand the differences in signal intensities obtained in polarization selective IR pump-probe spectroscopy, one can consider three scenarios. The first scenario is one in which an isotropic distribution of excited molecules is probed with a linearly polarized beam. [95-99] Evaluating the integral of these two distributions, with respect to volume, leads to a value of 1, shown as **Figure 5-5A**. The second scenario is one in which a cos θ distribution of excited molecules is probed by a parallel polarized beam, the integral of this would lead to a value of 1.8, shown as **Figure 5-5B**.[95-97] The final scenario is when a cos θ distribution is probed by a perpendicularly polarized beam, this integral presents a value of 0.6, as shown by **Figure 5.5C**.[95-97] Using these scenarios allows for determination of how the signals of the parallel and perpendicular probes will evolve in time, which can be seen below as equations 5-1 and 5-2. [95-97]

$$S_{||} = c_1(t)[1 + 0.8c_2(t)] \qquad (5\text{-}1)$$

$$S_{-} = c_1(t)[1 - 0.4c_2(t)] \qquad (5\text{-}2)$$

Where c_1 is the population correlation function, describing how the decay of the population evolves in time, and c_2 is the orientation correlation function, describing how the orientation evolves in time.[92-94, 97] It is a combination of these two contributions which produces the probe signal observed in polarization selective IR pump-probe measurements.[92-94, 97] To analyze the pure population decay or orientational dynamics, equations 5-3 and 5-4 can be used respectively to extract c_1 or c_2. For our experiment, we will focus on the use of equation 5-3, as it will allow us to obtain the orientational dynamics of the system.[86, 93]

$$0.4c_2(t) = \frac{S_{||} - S_{-}}{S_{||} + 2S_{-}} \qquad (5\text{-}3)$$

$$c_1(t) = \frac{1}{3}(S_{||} + 2S_{-}) \qquad (5\text{-}4)$$

It has been shown both experimentally and via simulations that at room temperature both the wobbling of MA^+ in $MAPbI_3$, and rotation about the N-N axis of FA^+ in $FAPbBr_3$ occur on the 100s of femtosecond (fs) timescale.[85, 91] While the reorientational jump between adjacent lattice faces occurs on the picosecond (ps) timescale.[85, 91] From these timescales we should expect to obtain data similar to figure 5-6, which possesses a fast decay component, due to the wobbling of MA^+ in $MAPbBr_3$ and the rotation about the N-N axis in $FAPbBr_3$, and a slow decay component in both samples due to the reorientational jump. Overall, we expect to fit the data with a biexponential decay function, shown as equation 5-5 below.[73, 85, 91]

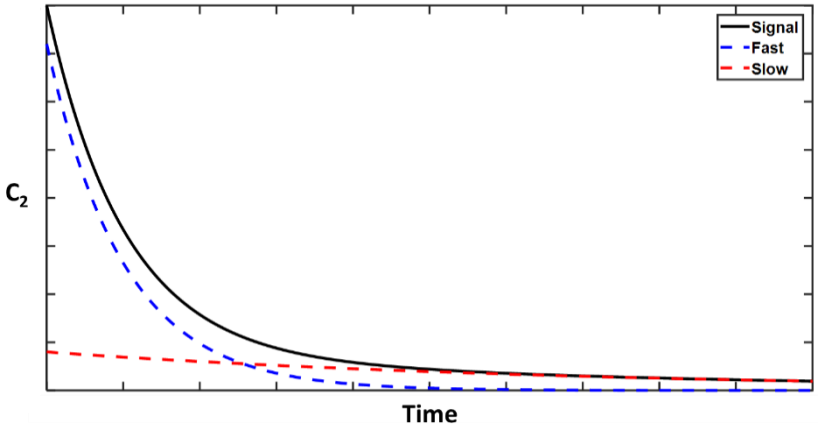

Figure 5-6: Example of biexponential decay used to fit anisotropy data. With fast and slow decay components shown separately.

$$A(t) = ae^{-k_1 t} + (1 - a)e^{-k_2 t} \qquad (5\text{-}5)$$

Where a is the initial population at time zero, k_1 and k_2 are the rate constants for the wobbling/rotation and jump respectively, and t is time.[73, 85, 91]

We will carry out our measurements at both room temperature and 80 K. This will allow us to ensure that the $MAPbBr_3$ sample has reached the orthorhombic phase, which is when the reorientational jump is frozen out and will allow us to make a comparison with $FAPbBr_3$.[73, 91] Our pump for these experiments will be ~1470 cm^{-1} for MA^+, which will excite the N-H bend, and ~1716 cm^{-1} for FA^+, which will excite the C-N stretch. We will then use a probe, which is red

shifted relative to each pump wavelength, to probe the 1→2 vibrational transition. **Figures 5-7A** and **5-7B** display the expected results for $MAPbBr_3$ and $FAPbBr_3$ respectively.

When directly comparing the room temperature anisotropy decays, we expect both the slow and fast decay components for $MAPbBr_3$ to be faster than in $FAPbBr_3$. The reason for this assumption is that at room temperature MA^+ is able to freely rotate, unlike FA^+, which is known to be rotationally hindered, leading us to believe it will have slower decays.[73, 87] Comparing the room temperature and 80 K decay rates of $MAPbBr_3$, we expect to see a transition from a biexponential decay to a monoexponential decay with a long lived tail.[87, 90] The reason for this transition is that, at room temperature, MA^+ is able to rotate freely, however, at 80 K the lattice is in its orthorhombic phase, which has been shown to greatly hinder the rotational freedom of MA^+.[87, 90] This rotational hindrance occurs to such a degree that the reorientational jump of MA^+ is no longer able to occur.[90] With this mode being lost it means that the cation will only be able to undergo the wobbling motion, which should present itself as a decay which can be fit with a single exponential and a long lived tail, due to the reorientational jump being unable to occur. [87, 90] Also, due to the restricted motion the rate constant for wobbling should decrease from room temperature to 80 K. For

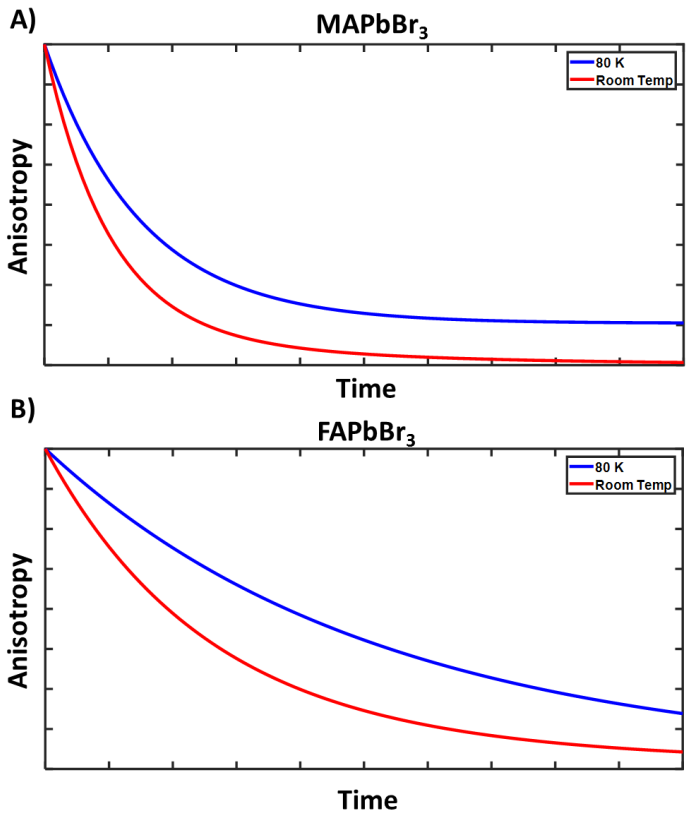

Figure 5-7: Predicted anisotropy decays at room temperature and 80 K for **A)** $MAPbBr_3$ and **B)** $FAPbBr_3$.

$FAPbBr_3$, we believe that the data will be able to be fit by biexponentials at both room temperature and 80 K.[85, 87, 90] Our reasoning for this assignment is because it has been inferred from theory, that the FA^+ rotational modes only show slight changes as temperature is lowered, as compared to the drastic changes that MA^+ undergoes.[87, 90] Along these same lines, we believe that while the rates of both FA^+ rotational modes will decrease, due to their increased restricted at lower temperatures, we do not expect to see as great a change as that of MA^+.[87, 90-91]

Once polarization selective IR pump-probe has been carried out in the ground state, we will transition to making the same measurements in the excited state. These excited state measurements will enable us to obtain an understanding of how the perovskite lattice's phonon modes change in the presence of charge carriers. It is well known in the field of photochemistry that the excited states of molecules behave very differently than their ground state counterparts, with the vibrational modes of the material changing, due to differences in the distribution of electron density and the different forces which act upon them.[51] In order to perform this measurement, we will use a visible pump (532 nm) to produce an excited state population, which will then be followed by a linearly polarized IR pump, and finally an IR probe, which will be polarized 45° relative to the IR pump. As before, we will carry out measurements at both room temperature and 80 K in order to see how phonon mode occupancy affects cations dynamics.

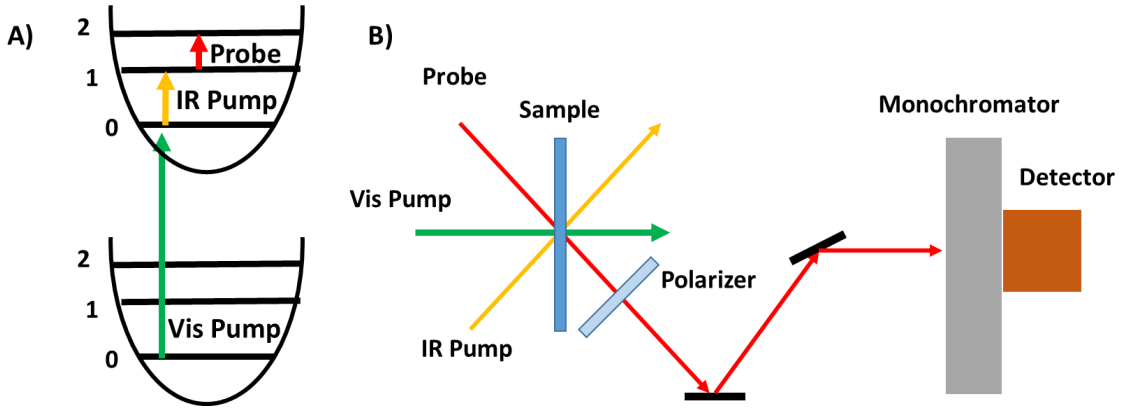

Figure 5-8: A) Energy level diagram for transitions affected using pump-pump-probe setup. **B)** Simplified visible pump IR pump-probe setup.

Figure 5-8A and **5-8B** represent the energy level diagram of the transitions and a simplified setup respectively.

One major consideration when attempting to carry out the excited state polarization selective IR pump-probe experiments, are the IR frequencies we will use. It is unlikely we will use the same frequencies that we used when carrying out the ground state variant of this experiment. The reason being, that the N-H bend of MA^+ at ~1470 cm^{-1} and the C-N stretch of FA^+ at ~1716 cm^{-1} lie on top of the large polaron absorption.[37-38] In order to avoid contributions from the polaron and Fano resonance, we will probe the N-H stretch mode of both MA^+ and FA^+ which lie in the 3000-3500 cm^{-1} region of the spectra.[37-38] Doing so will place the transient N-H stretch on the Drude-like tail of the polaron transition, which has a significantly smaller amplitude and shallower slope than in the 1000-2000 cm^{-1} region used in the TRIR measurements.[37-38] The lessened contribution from the polaron absorption will likely make interpretation of the data significantly easier, as there will be less of a contribution to the signal from the polaron absorption. However, since these vibrational modes are shifted further away from the polaron absorption than those previously used, they will likely have a smaller amplitude. This is because the coupling between the vibrational modes and the polaron will be lower, meaning the vibrations will not be able to obtain as high a degree of enhancement in oscillator strength as the previously used vibrations.

Comparison of the ground and excited state polarization dependent IR pump-probe measurements will allow us to obtain an even better understanding of how the material behaves in its excited state, which will be incredibly useful for the field.

TRIR Spectroscopy of $FAPbBr_3$ N-H Stretch

To ascertain whether the lack of hydrogen bonding between the molecular moiety we chose, and the lattice was part of the reason a shift in the transient vibrational spectra, at different temperatures, wasn't observed, we will perform TRIR spectroscopy on the N-H stretch of $FAPbBr_3$. As shown by **Figure 5-9** below, there is a collection of four vibrational peaks in the FTIR spectrum of $FAPbBr_3$, which lie between 3000 and 3500 cm^{-1}. Previous work has assigned these peaks to the N-H stretching modes of FA^+.[100] Using our TRIR spectroscopy setup mentioned previously, we will use a 532 nm visible pump, followed by a 3000 – 3500 cm^{-1} mid-IR probe. In order to see the affect that changes in the phonon mode occupancy have on the A site cation, we will measure spectra at both room temperature and 80 K, as this will allow for comparison of these data with the anisotropy experiments.

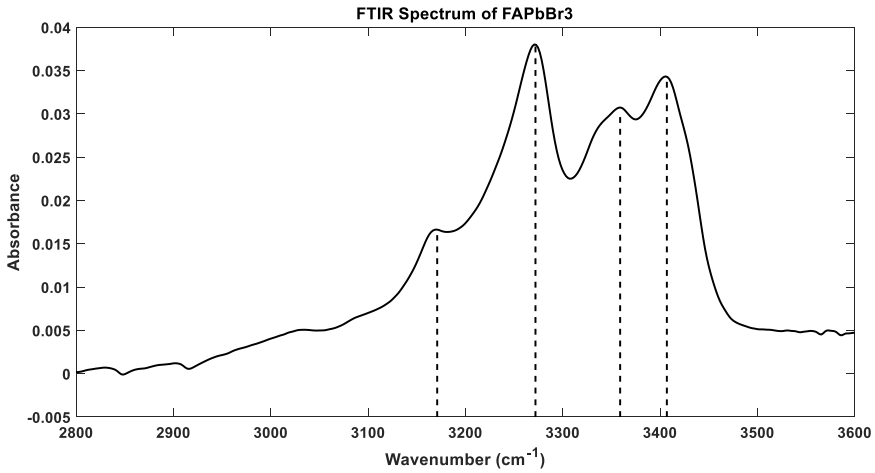

Figure 5-9: FTIR spectrum of $FAPbBr_3$, dotted lines are guide to the eye for the four vibrational modes mentioned.

We believe that there are two possible outcomes for this experiment, the predicted data for which can be seen as **Figure 5-10A** and **5-10B** below. The first scenario should produce a transient N-H stretch spectra which would not shift with temperature, and have a FWHM which would decrease as temperature was decreased, as depicted by **Figure 5-10A**. Since the dynamics of FA^+ are predicted to show little change with temperature, the N-H stretch may experience similar environments at both temperatures, which would cause the frequency of the vibration to stay the

same.[77] The decrease in FWHM as temperature is lowered could arise due to the amplitude of the phonon mode oscillations decreasing. This decrease in amplitude would lower the chance of FA^+ undergoing elastic collisions with the lattice, allowing it to retain its initial phase and frequency for a longer period of time, leading to a decrease in the dephasing time of the N-H stretch. The second scenario we are considering would produce a blue shift in the transient N-H spectra, and a decrease in FWHM as temperature was decreased, as depicted in **Figure 5-10B**. While the dynamics of FA^+ are theorized to not change drastically, they are still changing.[77] Thus, we believe it is possible that the changes in dynamics might be large enough that a shift in the N-H frequency between room temperature and 80 K could be observed. However, we believe that the shift would be smaller than that which would occur for $MAPbI_3$, as the dynamics of MA^+ change far more than those of FA^+.[77, 90] We also believe that the change in FWHM would be the same as mentioned for the first scenario.

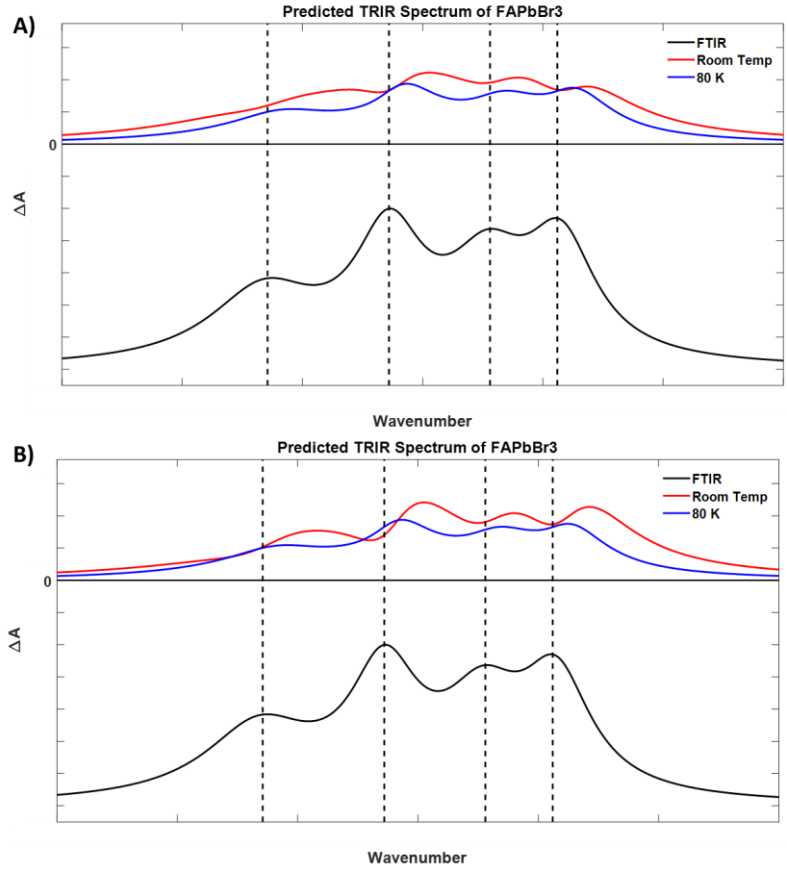

Figure 5-10: Predicted TRIR spectra for **A)** scenario 1 and **B)** scenario 2. Dotted lines are a guide to the eye showing the location of the peaks in the FTIR.

There are a number of characteristics about both sets of predicted data that should be noted. The first is the spectral region where these measurements will be made is on the higher frequency

edge of the Drude-like tail of the polaron spectrum. This part of the spectrum has a much lower amplitude absorption and a shallower slope, meaning that there is a much lower contribution to the signal from the polaron. This also means that we should not expect to see a Fano resonance in this region, as the transient vibration is significantly shifted from the continuum state. However, because the N-H stretch is significantly shifted from the polaron absorption, it will not have as high a degree of enhancement to its oscillator strength, as it will not be as coupled to the electronic transition of the polaron. Also because of the lower degree of enhancement, it is likely that the excited state absorption and the ground state bleach will have similar amplitudes, and both will contribute to the signal we observe. This means that the signal will likely have an irregular line shape, which we have included in our predicted data, that when fit will have to include peaks for the excited state absorption, and also the FTIR as a basis for the ground state bleach.

If our predictions for the polarization selective IR pump-probe and TRIR spectroscopy turn out to be correct, then it will prove that FA^+ does not undergo drastic changes in its dynamics as temperature is changed, unlike MA^+ which does. This would mean that the reason we see no shift in the transient C-N stretch of FA^+, is simply due to the fact that it has similar dynamics for the temperatures we measured. While the reason we see shifts in the transient N-H bend of MA^+, is due to the drastic changes in dynamics as the temperature is changed. This work could prove that the choice of A site cation matters when designing new perovskite materials. As it would infer, that the dynamics of both the cation and the lattice are more intimately connected than previously thought, and that while changing the A site cation doesn't lead to large changes in the band gap, it may drastically influence the phonon modes of the lattice.

References

1. Tang, H.; He, S.; Peng, C., A Short Progress Report on High-Efficiency Perovskite Solar Cells. *Nanoscale Res Lett* **2017,** *12* (1), 410-410.
2. Breeze, P., Solar Power Generation. Academic Press: 2016.
3. Ries, H. In *Thermodynamics of Solar Power Conversion*, Conference on Comparative Assessments of Solar Power Technologies, Jerusalem, Israel, February 1994; Solcom: Jerusalem, Israel, 1994; p 1.
4. Swanson, R. M. In *Approaching the 29% limit efficiency of silicon solar cells*, Conference Record of the Thirty-first IEEE Photovoltaic Specialists Conference, 2005., 3-7 Jan. 2005; 2005; pp 889-894.
5. Rühle, S., Tabulated values of the Shockley–Queisser limit for single junction solar cells. *Sol Energy* **2016,** *130*, 139-147.
6. Shockley, W.; Queisser, H. J., Detailed Balance Limit of Efficiency of p-n Junction Solar Cells. *J Appl Phys* **1961,** *32* (3), 510-519.
7. Glunz, S. W.; Preu, R.; Biro, D., 1.16 - Crystalline Silicon Solar Cells: State-of-the-Art and Future Developments. In *Comprehensive Renewable Energy*, Sayigh, A., Ed. Elsevier: Oxford, 2012; pp 353-387.
8. Best Research-Cell Efficiency Chart. https://www.nrel.gov/pv/cell-efficiency.html.
9. Battersby, S., News Feature: The solar cell of the future. *P Natl Acad Sci USA* **2019,** *116* (1), 7-10.
10. Green, M. A.; Hishikawa, Y.; Dunlop, E. D.; Levi, D. H.; Hohl-Ebinger, J.; Yoshita, M.; Ho-Baillie, A. W. Y., Solar cell efficiency tables (Version 53). *Progress in Photovoltaics: Research and Applications* **2019,** *27* (1), 3-12.
11. Razykov, T. M.; Ferekides, C. S.; Morel, D.; Stefanakos, E.; Ullal, H. S.; Upadhyaya, H. M., Solar photovoltaic electricity: Current status and future prospects. *Sol Energy* **2011,** *85* (8), 1580-1608.
12. Ceccaroli, B.; Ovrelid, E.; Pizzini, S., *Solar Silicon Processes*. Taylor and Franics Group[2017.
13. Gau, S. C.; Weinberger, B. R.; Akhtar, M.; Kiss, Z.; MacDiarmid, A. G., Preparation of amorphous silicon films by chemical vapor deposition from higher silanes SinH2n+2(n≳1). *Appl Phys Lett* **1981,** *39* (5), 436-438.
14. Kalogirou, S. A., Chapter 9 - Photovoltaic Systems. In *Solar Energy Engineering (Second Edition)*, Kalogirou, S. A., Ed. Academic Press: Boston, 2014; pp 481-540.
15. Green, M. A., Commercial progress and challenges for photovoltaics. *Nature Energy* **2016,** *1*, 15015.
16. Jena, A. K.; Kulkarni, A.; Miyasaka, T., Halide Perovskite Photovoltaics: Background, Status, and Future Prospects. *Chem Rev* **2019**.
17. Green, M. A.; Ho-Baillie, A.; Snaith, H. J., The emergence of perovskite solar cells. *Nature Photonics* **2014,** *8*, 506-514.
18. Manser, J. S.; Christians, J. A.; Kamat, P. V., Intriguing Optoelectronic Properties of Metal Halide Perovskites. *Chem Rev* **2016,** *116* (21), 12956-13008.
19. Chen, T.; Chen, W.-L.; Foley, B. J.; Lee, J.; Ruff, J. P. C.; Ko, J. Y. P.; Brown, C. M.; Harriger, L. W.; Zhang, D.; Park, C.; Yoon, M.; Chang, Y.-M.; Choi, J. J.; Lee, S.-H., Origin of long lifetime of band-edge charge carriers in organic–inorganic lead iodide perovskites. *Proceedings of the National Academy of Sciences* **2017,** *114* (29), 7519-7524.
20. Zuo, C.; Bolink, H. J.; Han, H.; Huang, J.; Cahen, D.; Ding, L., Advances in Perovskite Solar Cells. *Advanced Science* **2016,** *3* (7), 1500324-n/a.
21. Kojima, A.; Teshima, K.; Shirai, Y.; Miyasaka, T., Organometal Halide Perovskites as Visible-Light Sensitizers for Photovoltaic Cells. *Journal of the American Chemical Society* **2009,** *131* (17), 6050-6051.
22. Kazim, S.; Nazeeruddin, M. K.; Grätzel, M.; Ahmad, S., Perovskite as Light Harvester: A Game Changer in Photovoltaics. *Angewandte Chemie International Edition* **2014,** *53*, 2812-2824.

23. Herz, L. M., Charge-Carrier Dynamics in Organic-Inorganic Metal Halide Perovskites. *Annual Review of Physical Chemistry* **2016,** *67* (1), 65-89.
24. Li, Z.; Yang, M.; Park, J.-S.; Wei, S.-H.; Berry, J. J.; Zhu, K., Stabilizing Perovskite Structures by Tuning Tolerance Factor: Formation of Formamidinium and Cesium Lead Iodide Solid-State Alloys. *Chemistry of Materials* **2016,** *28* (1), 284-292.
25. Myung, C. W.; Yun, J.; Lee, G.; Kim, K. S., A New Perspective on the Role of A-Site Cations in Perovskite Solar Cells. *Advanced Energy Materials* **2018,** *8* (14), 1702898.
26. Targhi, F. F.; Jalili, Y. S.; Kanjouri, F., MAPbI3 and FAPbI3 perovskites as solar cells: Case study on structural, electrical and optical properties. *Results in Physics* **2018,** *10*, 616-627.
27. Frost, J. M.; Butler, K. T.; Brivio, F.; Hendon, C. H.; van Schilfgaarde, M.; Walsh, A., Atomistic Origins of High-Performance in Hybrid Halide Perovskite Solar Cells. *Nano Lett* **2014,** *14* (5), 2584-2590.
28. Huang, J.; Yuan, Y.; Shao, Y.; Yan, Y., Understanding the physical properties of hybrid perovskites for photovoltaic applications. *Nat Rev Mater* **2017,** *2* (7).
29. Zhu, X. Y.; Podzorov, V., Charge Carriers in Hybrid Organic-Inorganic Lead Halide Perovskites Might Be Protected as Large Polarons. *J Phys Chem Lett* **2015,** *6* (23), 4758-4761.
30. Miyata, A.; Mitioglu, A.; Plochocka, P.; Portugall, O.; Wang, J. T.-W.; Stranks, S. D.; Snaith, H. J.; Nicholas, R. J., Direct measurement of the exciton binding energy and effective masses for charge carriers in organic–inorganic tri-halide perovskites. *Nat Phys* **2015,** *11*, 582.
31. Chen, X.; Lu, H.; Yang, Y.; Beard, M. C., Excitonic Effects in Methylammonium Lead Halide Perovskites. *The Journal of Physical Chemistry Letters* **2018,** *9* (10), 2595-2603.
32. Bonn, M.; Miyata, K.; Hendry, E.; Zhu, X. Y., Role of Dielectric Drag in Polaron Mobility in Lead Halide Perovskites. *Acs Energy Letters* **2017,** *2* (11), 2555-2562.
33. Frost, J. M., Calculating polaron mobility in halide perovskites. *Physical Review B* **2017,** *96* (19).
34. Miyata, K.; Meggiolaro, D.; Trinh, M. T.; Joshi, P. P.; Mosconi, E.; Jones, S. C.; De Angelis, F.; Zhu, X. Y., Large polarons in lead halide perovskites. *Sci Adv* **2017,** *3* (8).
35. Emin, D., Optical-Properties of Large and Small Polarons and Bipolarons. *Physical Review B* **1993,** *48* (18), 13691-13702.
36. Alexandrov, A. S., Polarons in Advanced Materials. *Springer Ser Mater S* **2007,** *103*, 1-669.
37. Munson, K. T.; Kennehan, E. R.; Doucette, G. S.; Asbury, J. B., Dynamic Disorder Dominates Delocalization, Transport, and Recombination in Halide Perovskites. *Chem* **2018**.
38. Munson, K. T.; Doucette, G. S.; Kennehan, E. R.; Swartzfager, J. R.; Asbury, J. B., Vibrational Probe of the Structural Origins of Slow Recombination in Halide Perovskites. *The Journal of Physical Chemistry C* **2019,** *123* (12), 7061-7073.
39. Yin, T.; Fang, Y.; Fan, X.; Zhang, B.; Kuo, J.-L.; White, T. J.; Chow, G. M.; Yan, J.; Shen, Z. X., Hydrogen-Bonding Evolution during the Polymorphic Transformations in CH3NH3PbBr3: Experiment and Theory. *Chemistry of Materials* **2017,** *29* (14), 5974-5981.
40. Ivanovska, T.; Quarti, C.; Grancini, G.; Petrozza, A.; De Angelis, F.; Milani, A.; Ruani, G., Vibrational Response of Methylammonium Lead Iodide: From Cation Dynamics to Phonon–Phonon Interactions. *Chemsuschem* **2016,** *9* (20), 2994-3004.
41. Zhumekenov, A. A.; Saidaminov, M. I.; Haque, M. A.; Alarousu, E.; Sarmah, S. P.; Murali, B.; Dursun, I.; Miao, X.-H.; Abdelhady, A. L.; Wu, T.; Mohammed, O. F.; Bakr, O. M., Formamidinium Lead Halide Perovskite Crystals with Unprecedented Long Carrier Dynamics and Diffusion Length. *ACS Energy Letters* **2016,** *1* (1), 32-37.
42. Konstantakou, M.; Perganti, D.; Falaras, P.; Stergiopoulos, T., Anti-Solvent Crystallization Strategies for Highly Efficient Perovskite Solar Cells. *Crystals* **2017,** *7* (10).
43. Stewart, R. J.; Grieco, C.; Larsen, A. V.; Maier, J. J.; Asbury, J. B., Approaching Bulk Carrier Dynamics in Organo-Halide Perovskite Nanocrystalline Films by Surface Passivation. *The Journal of Physical Chemistry Letters* **2016,** *7*, 1148-1153.

44. Aydin, E.; De Bastiani, M.; De Wolf, S., Defect and Contact Passivation for Perovskite Solar Cells. *Advanced Materials* **2019,** *31* (25), 1900428.
45. Dequilettes, D. W.; Koch, S.; Burke, S.; Paranji, R.; Shropshire, A.; Ziffer, M.; Ginger, D. S., Photoluminescence Lifetimes Exceeding 8 μs and Quantum Yields Exceeding 30% in Hybrid Perovskite Thin Films by Ligand Passivation. *ACS Energy Letters* **2016**, 438-444.
46. Chen, B.; Rudd, P. N.; Yang, S.; Yuan, Y.; Huang, J., Imperfections and their passivation in halide perovskite solar cells. *Chem Soc Rev* **2019,** *48* (14), 3842-3867.
47. Munson, K. T.; Kennehan, E. R.; Asbury, J. B., Structural origins of the electronic properties of materials via time-resolved infrared spectroscopy. *J Mater Chem C* **2019,** *7* (20), 5889-5909.
48. Kennehan, E. R.; Doucette, G. S.; Marshall, A. R.; Grieco, C.; Munson, K. T.; Beard, M. C.; Asbury, J. B., Electron–Phonon Coupling and Resonant Relaxation from 1D and 1P States in PbS Quantum Dots. *ACS Nano* **2018,** *12* (6), 6263-6272.
49. Sezen, H.; Buchholz, M.; Nefedov, A.; Natzeck, C.; Heissler, S.; Di Valentin, C.; Wöll, C., Probing electrons in TiO2 polaronic trap states by IR-absorption: Evidence for the existence of hydrogenic states. *Sci Rep-Uk* **2014,** *4*, 3808.
50. Tkachenko, N. V., *Optical Spectroscopy: Methods and Instrumentations*. Elsevier Science: 2006; p 324.
51. Turro, N. J., *Modern Molecular Photochemistry*. University Science Books: California, 1991; p 628.
52. Atkins, P.; De Paula, J., *Atkins' Physical Chemistry*. 10th ed.; Oxford University Press: Oxford, 2014; p 1008.
53. Hollas, M. J., *Modern Spectroscopy*. 4th ed.; Wiley: 2010.
54. Grunwald, E.; Herzog, J.; Steel, C., Using Fourier Transforms to Understand Spectral Line Shapes. *Journal of Chemical Education* **1995,** *72* (3), 210.
55. Bradley, M. S.; Bratu, C., Vibrational Line Profiles as a Probe of Molecular Interactions. *Journal of Chemical Education* **1997,** *74* (5), 553.
56. Taj, S.; Baird, D.; Rosu-Finsen, A.; McCoustra, M. R. S., Surface heterogeneity and inhomogeneous broadening of vibrational line profiles. *Phys Chem Chem Phys* **2017,** *19* (11), 7990-7995.
57. Fano, U., Effects of Configuration Interaction on Intensities and Phase Shifts. *Physical Review* **1961,** *124* (6), 1866-1878.
58. Miroshnichenko, A. E.; Flach, S.; Kivshar, Y. S., Fano resonances in nanoscale structures. *Reviews of Modern Physics* **2010,** *82* (3), 2257-2298.
59. Luk'yanchuk, B.; Zheludev, N. I.; Maier, S. A.; Halas, N. J.; Nordlander, P.; Giessen, H.; Chong, C. T., The Fano resonance in plasmonic nanostructures and metamaterials. *Nature Materials* **2010,** *9*, 707.
60. Limonov, M. F.; Rybin, M. V.; Poddubny, A. N.; Kivshar, Y. S., Fano resonances in photonics. *Nature Photonics* **2017,** *11*, 543.
61. Agrawal, A.; Singh, A.; Yazdi, S.; Singh, A.; Ong, G. K.; Bustillo, K.; Johns, R. W.; Ringe, E.; Milliron, D. J., Resonant Coupling between Molecular Vibrations and Localized Surface Plasmon Resonance of Faceted Metal Oxide Nanocrystals. *Nano Lett* **2017,** *17* (4), 2611-2620.
62. Giannini, V.; Francescato, Y.; Amrania, H.; Phillips, C. C.; Maier, S. A., Fano Resonances in Nanoscale Plasmonic Systems: A Parameter-Free Modeling Approach. *Nano Lett* **2011,** *11* (7), 2835-2840.
63. Zhang, L.; Gogna, R.; Burg, W.; Tutuc, E.; Deng, H., Photonic-crystal exciton-polaritons in monolayer semiconductors. *Nature Communications* **2018,** *9* (1), 713.
64. Adato, R.; Artar, A.; Erramilli, S.; Altug, H., Engineered Absorption Enhancement and Induced Transparency in Coupled Molecular and Plasmonic Resonator Systems. *Nano Lett* **2013,** *13* (6), 2584-2591.
65. Joe, Y. S.; Satanin, A. M.; Kim, C. S., Classical analogy of Fano resonances. *Phys Scripta* **2006,** *74* (2), 259-266.
66. Kumar, R., Asymmetry to symmetry transition of Fano line-shape: analytical description. *Indian Journal of Physics* **2013,** *87* (1), 49-52.

67. Vogt, J.; Huck, C.; Neubrech, F.; Toma, A.; Gerbert, D.; Pucci, A., Impact of the plasmonic near- and far-field resonance-energy shift on the enhancement of infrared vibrational signals. *Phys Chem Chem Phys* **2015,** *17* (33), 21169-21175.
68. Nitzan, A.; Brus, L. E., Theoretical model for enhanced photochemistry on rough surfaces. *The Journal of Chemical Physics* **1981,** *75* (5), 2205-2214.
69. Dayal, G.; Chin, X. Y.; Soci, C.; Singh, R., High-Q Plasmonic Fano Resonance for Multiband Surface-Enhanced Infrared Absorption of Molecular Vibrational Sensing. *Adv Opt Mater* **2017,** *5* (2), 1600559.
70. Neubrech, F.; Huck, C.; Weber, K.; Pucci, A.; Giessen, H., Surface-Enhanced Infrared Spectroscopy Using Resonant Nanoantennas. *Chem Rev* **2017,** *117* (7), 5110-5145.
71. Qu, K.; Agarwal, G. S., Fano resonances and their control in optomechanics. *Phys Rev A* **2013,** *87* (6), 063813.
72. Govinda, S.; Kore, B. P.; Swain, D.; Hossain, A.; De, C.; Guru Row, T. N.; Sarma, D. D., Critical Comparison of FAPbX3 and MAPbX3 (X = Br and Cl): How Do They Differ? *The Journal of Physical Chemistry C* **2018,** *122* (25), 13758-13766.
73. Gallop, N. P.; Selig, O.; Giubertoni, G.; Bakker, H. J.; Rezus, Y. L. A.; Frost, J. M.; Jansen, T. L. C.; Lovrincic, R.; Bakulin, A. A., Rotational Cation Dynamics in Metal Halide Perovskites: Effect on Phonons and Material Properties. *The Journal of Physical Chemistry Letters* **2018,** *9* (20), 5987-5997.
74. Ma, F.; Li, J.; Li, W.; Lin, N.; Wang, L.; Qiao, J., Stable α/δ phase junction of formamidinium lead iodide perovskites for enhanced near-infrared emission. *Chemical Science* **2017,** *8* (1), 800-805.
75. Rehman, W.; Milot, R. L.; Eperon, G. E.; Wehrenfennig, C.; Boland, J. L.; Snaith, H. J.; Johnston, M. B.; Herz, L. M., Charge-Carrier Dynamics and Mobilities in Formamidinium Lead Mixed-Halide Perovskites. *Advanced Materials* **2015,** *27* (48), 7938-7944.
76. Wright, A. D.; Verdi, C.; Milot, R. L.; Eperon, G. E.; Pérez-Osorio, M. A.; Snaith, H. J.; Giustino, F.; Johnston, M. B.; Herz, L. M., Electron–phonon coupling in hybrid lead halide perovskites. *Nature Communications* **2016,** *7*, 11755.
77. Davies, C. L.; Borchert, J.; Xia, C. Q.; Milot, R. L.; Kraus, H.; Johnston, M. B.; Herz, L. M., Impact of the Organic Cation on the Optoelectronic Properties of Formamidinium Lead Triiodide. *The Journal of Physical Chemistry Letters* **2018,** *9* (16), 4502-4511.
78. Yamada, Y.; Nakamura, T.; Endo, M.; Wakamiya, A.; Kanemitsu, Y., Photocarrier Recombination Dynamics in Perovskite CH3NH3PbI3 for Solar Cell Applications. *Journal of the American Chemical Society* **2014,** *136* (33), 11610-11613.
79. Tvingstedt, K.; Malinkiewicz, O.; Baumann, A.; Deibel, C.; Snaith, H. J.; Dyakonov, V.; Bolink, H. J., Radiative efficiency of lead iodide based perovskite solar cells. *Sci Rep-Uk* **2014,** *4*, 6071.
80. Dai, J.; Zheng, H.; Zhu, C.; Lu, J.; Xu, C., Comparative investigation on temperature-dependent photoluminescence of CH3NH3PbBr3 and CH(NH2)2PbBr3 microstructures. *J Mater Chem C* **2016,** *4* (20), 4408-4413.
81. Gélvez-Rueda, M. C.; Renaud, N.; Grozema, F. C., Temperature Dependent Charge Carrier Dynamics in Formamidinium Lead Iodide Perovskite. *The Journal of Physical Chemistry C* **2017,** *121* (42), 23392-23397.
82. Weller, M. T.; Weber, O. J.; Henry, P. F.; Di Pumpo, A. M.; Hansen, T. C., Complete structure and cation orientation in the perovskite photovoltaic methylammonium lead iodide between 100 and 352 K. *Chem Commun* **2015,** *51* (20), 4180-4183.
83. Quarti, C.; Mosconi, E.; Ball, J. M.; D'Innocenzo, V.; Tao, C.; Pathak, S.; Snaith, H. J.; Petrozza, A.; De Angelis, F., Structural and optical properties of methylammonium lead iodide across the tetragonal to cubic phase transition: implications for perovskite solar cells. *Energy & Environmental Science* **2016,** *9* (1), 155-163.

84. Chen, Y.; Yi, H. T.; Wu, X.; Haroldson, R.; Gartstein, Y. N.; Rodionov, Y. I.; Tikhonov, K. S.; Zakhidov, A.; Zhu, X. Y.; Podzorov, V., Extended carrier lifetimes and diffusion in hybrid perovskites revealed by Hall effect and photoconductivity measurements. *Nature Communications* **2016,** *7*, 12253.
85. Taylor, V. C. A.; Tiwari, D.; Duchi, M.; Donaldson, P. M.; Clark, I. P.; Fermin, D. J.; Oliver, T. A. A., Investigating the Role of the Organic Cation in Formamidinium Lead Iodide Perovskite Using Ultrafast Spectroscopy. *The Journal of Physical Chemistry Letters* **2018,** *9* (4), 895-901.
86. Lee, C.; Son, H.; Park, S., Effect of Hydrogen Bonds on the Vibrational Relaxation and Orientational Relaxation Dynamics of HN3 and N3– in Solutions. *The Journal of Physical Chemistry B* **2016,** *120* (36), 9723-9731.
87. Maheshwari, S.; Fridriksson, M. B.; Seal, S.; Meyer, J.; Grozema, F. C., The Relation between Rotational Dynamics of the Organic Cation and Phase Transitions in Hybrid Halide Perovskites. *The Journal of Physical Chemistry C* **2019,** *123* (23), 14652-14661.
88. Leguy, A. M. A.; Frost, J. M.; McMahon, A. P.; Sakai, V. G.; Kockelmann, W.; Law, C.; Li, X.; Foglia, F.; Walsh, A.; O'Regan, B. C.; Nelson, J.; Cabral, J. T.; Barnes, P. R. F., The dynamics of methylammonium ions in hybrid organic–inorganic perovskite solar cells. *Nature Communications* **2015,** *6*, 7124.
89. Zhang, Z.; Long, R.; Tokina, M. V.; Prezhdo, O. V., Interplay between Localized and Free Charge Carriers Can Explain Hot Fluorescence in the CH3NH3PbBr3 Perovskite: Time-Domain Ab Initio Analysis. *Journal of the American Chemical Society* **2017,** *139* (48), 17327-17333.
90. Chen, T.; Foley, B. J.; Ipek, B.; Tyagi, M.; Copley, J. R. D.; Brown, C. M.; Choi, J. J.; Lee, S.-H., Rotational dynamics of organic cations in the CH3NH3PbI3 perovskite. *Phys Chem Chem Phys* **2015,** *17* (46), 31278-31286.
91. Selig, O.; Sadhanala, A.; Müller, C.; Lovrincic, R.; Chen, Z.; Rezus, Y. L. A.; Frost, J. M.; Jansen, T. L. C.; Bakulin, A. A., Organic Cation Rotation and Immobilization in Pure and Mixed Methylammonium Lead-Halide Perovskites. *Journal of the American Chemical Society* **2017,** *139* (11), 4068-4074.
92. Kramer, P. L.; Nishida, J.; Fayer, M. D., Separation of experimental 2D IR frequency-frequency correlation functions into structural and reorientation-induced contributions. *The Journal of Chemical Physics* **2015,** *143* (12), 124505.
93. Park, S.; Fayer, M. D., Hydrogen bond dynamics in aqueous NaBr solutions. *Proceedings of the National Academy of Sciences* **2007,** *104* (43), 16731-16738.
94. Moilanen, D. E.; Fenn, E. E.; Wong, D.; Fayer, M. D., Water dynamics in large and small reverse micelles: from two ensembles to collective behavior. *The Journal of chemical physics* **2009,** *131* (1), 014704-014704.
95. Moilanen, D. E.; Fenn, E. E.; Wong, D.; Fayer, M. D., Geometry and Nanolength Scales versus Interface Interactions: Water Dynamics in AOT Lamellar Structures and Reverse Micelles. *Journal of the American Chemical Society* **2009,** *131* (23), 8318-8328.
96. Tan, H.-S.; Piletic, I. R.; Fayer, M. D., Polarization selective spectroscopy experiments: methodology and pitfalls. *J. Opt. Soc. Am. B* **2005,** *22* (9), 2009-2017.
97. Woutersen, S.; Emmerichs, U.; Bakker, H. J., Femtosecond Mid-IR Pump-Probe Spectroscopy of Liquid Water: Evidence for a Two-Component Structure. *Science* **1997,** *278* (5338), 658-660.
98. Kurochkin, D. V.; Naraharisetty, S. R. G.; Rubtsov, I. V., A relaxation-assisted 2D IR spectroscopy method. *Proceedings of the National Academy of Sciences* **2007,** *104* (36), 14209-14214.
99. Hochstrasser, R. M., Two-dimensional IR-spectroscopy: polarization anisotropy effects. *Chemical Physics* **2001,** *266* (2), 273-284.
100. Hills-Kimball, K.; Nagaoka, Y.; Cao, C.; Chaykovsky, E.; Chen, O., Synthesis of formamidinium lead halide perovskite nanocrystals through solid–liquid–solid cation exchange. *J Mater Chem C* **2017,** *5* (23), 5680-5684.